The Role of Slab Remnants in Modulating Free Subduction Dynamics: a 3-D Spherical Numerical Study

Fangqin Chen[1], D. Rhodri Davies[1], Saskia Goes[2], Lior Suchoy[2], Stephan C. Kramer[2]

[1]Research School of Earth Sciences, The Australian National University, Canberra, ACT, Australia
[2]Department of Earth Science and Engineering, Imperial College London, London, UK

Key Points:

- Subducted slab remnants can enhance the sinking velocities of actively subducting plates by up to a factor 2.
- Slab remnants strongly influence trench motions and the evolution of trench shape at subduction zones located within a few 100 to 1000 km.
- The flow fields interact such that the slab tip and remnant approach, thus strengthening mantle flow that can anchor subduction location.

Corresponding author: Rhodri Davies, Rhodri.Davies@anu.edu.au

Abstract

Seismic tomography of Earth's mantle images abundant slab remnants, often located in close proximity to active subduction systems. The impact of such remnants on the dynamics of subduction remains underexplored. Here, we use simulations of multi-material free subduction in a 3-D spherical shell geometry to examine the interaction between viscoplastic slabs and remnants that are positioned above, within and below the mantle transition zone. Depending on their size, negatively buoyant remnants can set up mantle flow of similar strength and length scales as that due to active subduction. As such, we find that remnants located within a few hundred km from a slab tip can locally enhance sinking by up to a factor 2. Remnant location influences trench motion: the trench advances towards a remnant positioned in the mantle wedge region, whereas remnants in the subslab region enhance trench retreat. These motions aid in rotating the subducting slab and remnant towards each other, reducing the distance between them, and further enhancing the positive interaction of their mantle flow fields. In this process, the trench develops along-strike variations in shape that are dependent on the remnant's location. Slab-remnant interactions may explain the poor correlation between subducting plate velocities and subducting plate age found in recent plate tectonic reconstructions. Our results imply that slab-remnant interactions affect the evolution of subducting slabs and trench geometry. Remnant-induced downwelling may also anchor and sustain subduction systems, facilitate subduction initiation, and contribute to plate reorganisation events.

Plain Language Summary

Subduction, the process where cold oceanic lithosphere descends into the mantle, is a time-dependent process: old subduction zones cease while new subduction zones initiate, in cycles of tectonic plate motions. The cessation of subduction is accompanied by break-off of the subducting slab from the surface plate, forming a slab remnant. The remnant continues sinking into the mantle and, in doing so, generates a flow field that may influence adjacent subduction systems. In this study, we present numerical simulations of subduction in a 3-D spherical shell domain, and examine how subduction systems interact with a range of slab remnants. Our models show that sinking remnants can significantly enhance the sinking velocity of slabs within a few 100-1000 km of the remnants, and can influence the spatial and temporal evolution of trench shape. Our results suggest that the existence of slab remnants may help to anchor and sustain subduction systems, and lead to an environment more favourable for the initiation of new subduction zones. Since such events are closely linked to reorganisations in global plate motions, we suggest that the location of pre-existing remnants influences tectonic plate movements and, potentially, super continent cycles.

1 Introduction

Subducting slabs are a key driver of mantle flow and surface plate motions (e.g., Forsyth & Uyeda, 1975; Lithgow-Bertelloni & Richards, 1998; Becker & O'Connell, 2001). Images of fast seismic velocity anomalies extending to depth, alongside Earth's long-wavelength geoid expression, imply that slabs regularly sink to the core-mantle-boundary (CMB), organising deep mantle structure as they descend (e.g. Hager, 1984; Grand et al., 1997; van der Hilst et al., 1997; D. R. Davies et al., 2012; Rubey et al., 2017; Ghelichkhan et al., 2021; D. R. Davies et al., 2023).

Seismic observations, however, suggest that subducting slabs are very rarely continuous over the mantle's entire depth extent. Tomography and seismicity point towards a prevalence of slab gaps, slab tears and detached slab fragments across the globe. An abundance of slab remnants associated with recent subduction systems are imaged above and within the mantle transition zone (MTZ) (e.g. Li et al., 2008; Simmons et al., 2012; Fukao & Obayashi, 2013; Wei et al., 2015; Goes et al., 2017; van der Meer et al., 2018;

Lei et al., 2020), with older remnants imaged at greater depths, relating, for example, to former Tethyan (e.g. Grand et al., 1997; Bijwaard et al., 1998; van der Voo et al., 1999; Bunge et al., 2002; Replumaz et al., 2004; Hafkenscheid et al., 2006; Fukao et al., 2009; Becker & Faccenna, 2011; van der Meer et al., 2018) and Farallon (e.g. Grand et al., 1997; Bijwaard et al., 1998; van der Hilst et al., 1997; Zhao, 2004; Sigloch et al., 2008; Fukao et al., 2009; van der Meer et al., 2018) subduction systems.

The existence of remnants requires slab detachment or break-off, with several mechanisms proposed. In plate reorganisation events, trenches may be abandoned, with the connected slab eventually detaching from the surface plate (e.g., Whittaker et al., 2007; Matthews et al., 2012; Müller et al., 2016). The arrival of an active spreading centre or buoyant continental lithosphere at the trench can also induce subduction termination (e.g., J. H. Davies & von Blanckenburg, 1995; Wong A Ton & Wortel, 1997; Wortel & Spakman, 2000; Faccenna et al., 2006; Burkett & Billen, 2009; Duretz et al., 2014; Seton et al., 2015). Furthermore, the subduction of faults or buoyant anomalies can facilitate slab tearing (e.g., Thorkelson & Taylor, 1989; Abratis & Wörner, 2001; Pallares et al., 2007), which can also occur to accommodate changes in plate geometry, as postulated for STEP faults (e.g. Thorkelson, 1996; Govers & Wortel, 2005; Obayashi et al., 2009). Following break off from their active subduction systems, the negative buoyancy and rheological properties of remnants make it likely that they continue to influence mantle convection and the dynamics of nearby active subduction systems. The dynamics of such interactions, however, has not yet been systematically examined.

In this paper, we investigate how actively subducting slabs interact with, and are influenced by slab remnants, above, within, and below the mantle transition zone. We focus on this depth range for two reasons: (i) whilst slabs sink through the upper mantle in a few million years, they can stagnate within the MTZ for tens of millions of years in response to phase buoyancy, rheological complexities, and a likely viscosity increase at these depths (e.g. Ringwood, 1975; Christensen & Yuen, 1984; Tackley et al., 1993; Karato et al., 2001; Garel et al., 2014; Goes et al., 2017; Čížková & Bina, 2019); and (ii) slab-transition zone interaction strongly affects the subduction mode and thus controls the surface expressions of subduction systems, for example through plate motions and the evolution of trench shape (e.g., Torii & Yoshioka, 2007; Ribe, 2010; Stegman et al., 2010; Garel et al., 2014; Goes et al., 2017; Cerpa et al., 2022).

Slab remnants are frequently imaged around the MTZ, most in close proximity to active subduction systems (Figure 1). Remnants from the extensive Farallon and adjacent plates have been imaged beneath North and South America (e.g. van der Lee & Nolet, 1997; Sigloch et al., 2008; van Benthem et al., 2013). Proto-Caribbean slab fragments have been identified at $\sim$ 1000 km depth below northeastern South America by combining seismic tomography and plate reconstructions (e.g. van Benthem et al., 2013; Braszus et al., 2021). Tethyan slab fragments have been found over a large area, extending from beneath the Mediterranean to India, across a range of depths (e.g. Wortel & Spakman, 2000; Hafkenscheid et al., 2006). South-east Asia has a complex subduction history resulting in a multitude of interacting slabs and remnants (e.g. Li et al., 2008; Hall & Spakman, 2015; van der Meer et al., 2018). Proto-South China Sea Plate remnants have been imaged in the lower mantle beneath Northern Borneo (e.g. Zahirovic et al., 2014; Hall & Spakman, 2015; Wu & Suppe, 2018; Pilia et al., 2023); Wu and Suppe (2018) further suggest that northern remnants of the Proto-South China Sea plate are stagnating at the transition zone under the South China Sea, adjacent to the slab currently subducting at the Manila trench. To the east of the region, subducted remnants of the Philippine Sea plate can be inferred from tomography at $\sim$ 800 km depth, in agreement with the reconstructed locations of major subduction zones in the region at 30 Ma (e.g. Widiyantoro et al., 2011; Hall & Spakman, 2015). A relic of the Kula slab is interpreted to be stagnating above the transition zone beneath the Bering Sea, just to the north of where the Pacific Plate subducts at the Aleutian trench (e.g. Gorbatov et al., 2000; van der

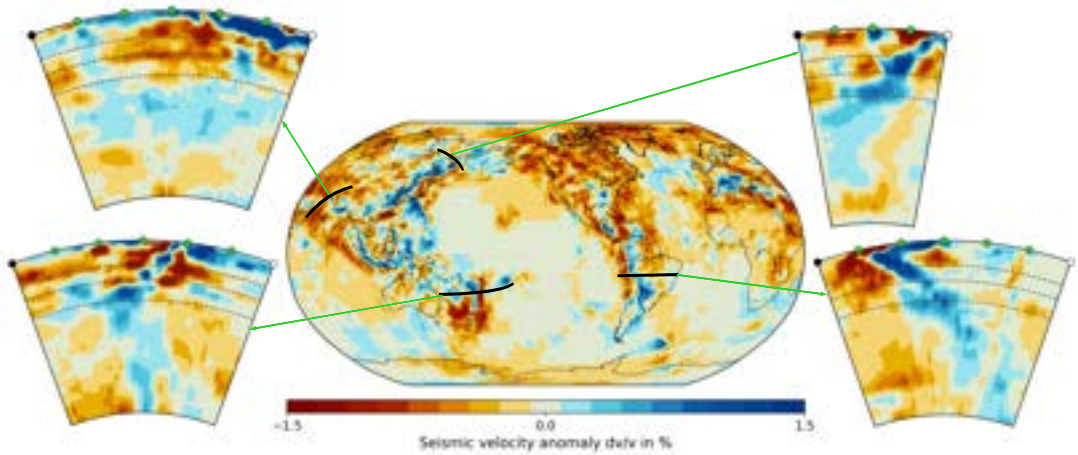

Figure 1. P-wave velocity anomalies at 660 km depth from UU-P07 tomography model (Amaru, 2007). Whole mantle cross-sections of Tethyan, Kula, Farallon, and Melanesia slab remnants are illustrated in clockwise order from top left. Dashed lines in cross-sections mark 410, 660, and 1000 km depth,respectively.

Meer et al., 2018). Flat lying slab remnants in the transition zone, proposed to be from Paleogene Pacific subduction at the Melanesia Arc, have been imaged in close proximity to current Tongan subduction (e.g. Hall & Spakman, 2002; Pysklywec et al., 2003). There are, therefore, many examples of slabs subducting into a region of the mantle with pre-existing remnants.

The most often discussed effect of remnants on subduction systems is tectonic plate reorganisation. Pysklywec and Ishii (2005) studied the effect of slab remnants on the dynamics of active subduction using a suite of 2-D numerical models, finding that they can either drive trench retreat or induce slab detachment and a reversal of subduction polarity, depending on remnant location relative to the trench. This mechanism may contribute to tectonic plate reorganisation events, where Pysklywec et al. (2003) suggest that the subducted Tonga slab may have caused detachment of the Vitiaz slab and initiation of subduction at the New Hebrides Trench. It has also been suggested that remnant-induced downwelling flow may play a role in subduction initiation (Crameri et al., 2020), that mantle flow induced by slab remnants influences the dip of adjacent subduction systems (Hu & Gurnis, 2020), and that the flow-field driven by remnants may facilitate the opening of intra-plate basins (e.g., Pysklywec & Mitrovica, 1999; Capitanio et al., 2009; Yang et al., 2018). Remnants also play a role in driving and modulating large-scale mantle flow, which will ultimately influence the dip and orientation of subducting slabs, trench migration rates and upper plate deformation (e.g., Hager & O'Connell, 1979; Husson, 2012; Ficini et al., 2017; Chertova et al., 2018; Stotz et al., 2018; Holt & Royden, 2020). Despite this, a systematic study into how the dynamics of subduction are influenced by slab remnants (and vice versa) has not yet been undertaken. Furthermore, the effects of a 3-D spherical shell domain, which constrains the space available for mantle flow (F. Chen et al., 2022a), on slab-remnant interaction, have not previously been considered.

In this study, we fill this gap by investigating the effect of slab remnants on the dynamics of subducting slabs and the evolution of subduction systems in a 3-D spherical shell domain. We build on seismic tomography observations of remnant slabs (e.g., Li et al., 2008; van der Meer et al., 2018) and previous models (e.g. Pysklywec & Ishii, 2005), and simulate the interaction between remnant slabs and subduction zones through a suite

of 3-D spherical shell cases, using the modelling approach developed in F. Chen et al. (2022a, 2022b).

Like freely subducting slabs (Capitanio et al., 2007; Ribe, 2010), remnants act as Stokes sinkers, as they have viscosities that are orders of magnitude higher than the surrounding mantle limiting their deformation (e.g., Jarvis & Lowman, 2007; Quéré et al., 2013). The velocity of slab-like vertical ellipsoid Stokes sinkers depends on their shape, density and the viscosity of surrounding material as follows (Capitanio et al., 2007):

$$v_{\text{Stokes}} = \frac{hL\Delta\rho}{12\sqrt{2}\mu} \times \frac{W}{L} \times \frac{1}{1+\log(\frac{W}{L})} \tag{1}$$

where $\Delta\rho$ is the density difference between slab/remnant and the adjacent mantle, μ is the viscosity of the surrounding mantle, and h, W, and L are plate thickness, along-strike width and down-dip length, respectively. We vary remnant density, shape and size, allowing us to examine the impact of remnants with different sinking velocities and associated mantle flow fields. Subducting slabs set up significant mantle flow around them to distances of approximately slab half width, up to 1000-1500 km in along-strike direction and on the order of their slab length in trench-perpendicular directions (distances dependent on mantle viscosity) (Piromallo et al., 2006; Schellart et al., 2007; F. Chen et al., 2022b). Sinking remnant slabs are expected to set up mantle flow of similar flow strength and scales. The flow regime induced by a sinking remnant will thus exert forces on nearby subduction systems, the impact of which not only depends on remnant properties, but also on remnant location relative to the subducting plate. Accordingly, we also vary remnant location and orientation relative to the trench, placing remnants at different distances from the slab, below the mantle wedge, the slab tip, and the sub-slab regions. In addition, to isolate the role of remnant buoyancy, we examine whether the presence of a purely viscous remnant (i.e. a remnant with no buoyancy anomaly relative to adjacent mantle) can alter the flow regime and dynamics of an active subduction system.

In the following sections, we first describe the setup of our numerical models, including the governing equations, the initial geometric configurations, boundary conditions and material properties, and summarise the different cases examined. We then quantitatively analyse our models to reveal: (i) how remnant density influences the dynamics of adjacent subduction zones; (ii) how remnant location and orientation modulate their effects; and (iii) how remnants of different dimensions influence trenches of different width. We end by discussing the implications of our results, and explore their applicability for understanding interactions between slab remnants and active subduction zones on Earth.

2 Computational Approach

2.1 Governing Equations and Numerical Strategy

We simulate free subduction of a composite visco-plastic plate into ambient underlying mantle inside a 3-D spherical shell domain using a multi material approach. In cases where we can exploit the symmetry of the system, our simulations are undertaken in a hemispherical shell, following F. Chen et al. (2022b). Assuming incompressibility, the governing equations for this problem are the continuity equation,

$$\nabla \cdot \mathbf{u} = 0, \tag{2}$$

the conservation of momentum equation at infinite Prandtl number,

$$-\nabla p + \nabla \cdot \left[\mu \left(\nabla \mathbf{u} + (\nabla \mathbf{u})^T\right)\right] = g\Delta\rho\Gamma\hat{k} \tag{3}$$

and an advection equation for tracking different materials,

$$\frac{\partial \Gamma}{\partial t} + \mathbf{u} \cdot \nabla \Gamma = 0, \tag{4}$$

In the above equations, $\mathbf{u}$ represents velocity, p pressure, μ viscosity, ρ density, g gravitational acceleration, $\hat{k}$ the unit vector in the direction opposite to gravity, and Γ the material volume fraction ($\Gamma = 1$ in a region occupied by a given material and $\Gamma = 0$ elsewhere). At material interfaces, the average viscosity is calculated through a geometric mean,

$$\mu_{\text{ave}} = \mu_1^{\Gamma_1} \mu_2^{\Gamma_2}, \tag{5}$$

where μ_i is the viscosity of material i, and Γ_i is the relative volume fraction of material i in the vicinity of the finite-element node at which the effective viscosity μ_{ave} is needed.

Simulations are undertaken using Fluidity (e.g., D. R. Davies et al., 2011; Kramer et al., 2012; Le Voci et al., 2014; D. R. Davies et al., 2016; Kramer, Davies, & Wilson, 2021), an adaptive, anisotropic, unstructured-mesh finite element and control volume computational modelling framework, capable of efficiently simulating multi-material whole-mantle visco-plastic (Tosi et al., 2015) subduction in spherical shell geometries (F. Chen et al., 2022a, 2022b). Fluidity's adaptive mesh capabilities allow our simulations to achieve a local resolution of $\sim$ 3 km in regions of dynamical significance, with coarser resolution of up to ~ 300 km elsewhere.

The importance of sphericity in simulating the dynamics of subduction, particularly for wider subduction systems, has been demonstrated by F. Chen et al. (2022a), who identify two key limitations of Cartesian compared to spherical models: (i) the presence of sidewall boundaries in Cartesian models, which modify the flow regime; and (ii) the reduction of space with depth in spherical shells, alongside the radial gravity direction, which cannot be captured in Cartesian domains. This motivates the use of spherical models herein.

2.2 Geometry, Boundary Conditions and Material Properties

The configuration of our reference models without remnants (cases W2400 and W4800) follows the setup of F. Chen et al. (2022a) for a subducting plate with plate buoyancy and thickness in the mid-range for natural subduction (cases S_W2400 and S_W4800, respectively). Simulations are undertaken in a hemispherical shell domain (thus exploiting the symmetry of the system to halve the computational domain's extent) with outer and inner radii that correspond to Earth's surface and CMB (Figure 2a). A free-surface boundary condition is applied on the outer surface, with free-slip conditions on the symmetric mid-plane and CMB. Gravity points radially towards the centre of the sphere. A factor of 50 viscosity increase is included at 660 km depth. Parameters common to all simulations are listed in Table 1.

The subducting plate has length $L = 2200$ km, thickness $h = 70$ km and a density contrast with adjacent mantle of $\Delta\rho = 80$ kg m^{-3}. Highly viscous side plates that cover the entire domain adjacent to the subducting plate are required to prevent the undesired narrowing effect on the subducting plate from shallow lateral flow (as in Holt et al., 2017). The initial slab tip geometry is prescribed with a bending radius of 250 km and an angle of 77° (Figure 2b), following F. Chen et al. (2022b). The subducting lithosphere is a composite plate comprising a core isoviscous layer (thickness $h_c = 30$ km) embedded in upper and lower visco-plastic layers with viscosities following a von Mises law, building on OzBench et al. (2008). Upper and lower plates are assigned the minimum viscosity between the Newtonian viscosity μ_{Newt} and an effective von Mises viscosity μ_{vM}, such that purely viscous deformation occurs when the second invariant of the stress tensor $\tau_{\text{II}} = 2\mu\dot{\varepsilon}_{\text{II}}$ (where $\dot{\varepsilon}_{\text{II}}$ is the second invariant of strain rate tensor) is below the critical yield stress, τ_{yield}. The effective viscosity of visco-plastic layers is given

Table 1. Parameters common to all simulations.

Parameter	Symbol	Value
Gravitational acceleration	g	$10\ \mathrm{m\,s^{-2}}$
Characteristic depth (whole mantle)	H	2890 km
Depth of upper mantle	H_{um}	660 km
Plate thickness	h	70 km
Core plate thickness	h_{c}	30 km
Plate length	L	2200 km
Remnant thickness	h_{rem}	70 km
Remnant length	L_{rem}	400 km
Upper mantle reference viscosity	μ_{um}	2.0×10^{20} Pa s
Lower mantle reference viscosity	μ_{lm}	$50 \times \mu_{\mathrm{um}}$
Core plate viscosity	μ_{cp}	$100 \times \mu_{\mathrm{um}}$
Initial viscosity of visco-plastic layer	μ_{Newt}	$100 \times \mu_{\mathrm{um}}$
Side plate viscosity	μ_{sp}	$1000 \times \mu_{\mathrm{um}}$
Remnant viscosity	μ_{rem}	$100 \times \mu_{\mathrm{um}}$
Mantle density	ρ	$3300\ \mathrm{kg\,m^{-3}}$
Plate density contrast	$\Delta\rho$	$80\ \mathrm{kg\,m^{-3}}$
Yield stress	τ_{yield}	100 MPa

by:

$$\mu_{\mathrm{vM}} = \begin{cases} \frac{\tau_{\mathrm{II}}}{2\dot{\varepsilon}_{\mathrm{II}}}, & \text{if } \tau < \tau_{\mathrm{yield}} \\ \frac{\tau_{\mathrm{yield}}}{2\dot{\varepsilon}_{\mathrm{II}}}, & \text{if } \tau \geq \tau_{\mathrm{yield}} \end{cases} \tag{6}$$

We simulate a wide-range of remnant cases, assuming a region of pre-existing isoviscous plate-like material in the mantle with a thickness (h_{rem}) of 70 km and a length (L_{rem}) of 400 km. For symmetric cases, remnants are designed to either have the same, or half, the subducting plate width, as illustrated in Figure 2(c). The remnant can be horizontally (Figure 2d) or radially oriented (Figure 2e). When horizontally oriented, remnants can occupy three positions: (a) *sub-slab*, where the remnant is offset 500 km laterally from the initial trench location beneath the downgoing plate (at a horizontal distance of ∼700 km from the slab tip); (b) *under*, where the remnant is placed directly below the initial trench location; and (c) *wedge*, where the remnant is offset 500 km from the initial trench in the mantle wedge direction (at a horizontal distance of ∼300 km from the slab tip: Figure 2d). In asymmetric cases, remnants are horizontally oriented in either the *under* or *wedge* location, with the key difference being that the centre of the remnant is not aligned with the centre of the subducting plate, as illustrated in Figure 2(g/h).

2.3 Cases Examined and Quantitative Model Diagnostics

We investigate a total of 17 cases, 15 of which are symmetric, with varying plate width (w), remnant width (w_{rem}), remnant orientation, remnant position, remnant depth (D_{rem} – denoting its deepest point), and density contrast between remnant and ambient mantle ($\Delta\rho_{\mathrm{rem}}$). In the following sections, the widths specified refer to the full widths of the plate or remnant, but in practice, for symmetric cases, we only simulate half of the width.

Our choice of reference plate widths of 2400 and 4800 km is motivated by results from F. Chen et al. (2022b), which show that at a width of 2400 km the subducting slab behaves relatively uniformly along-strike, but at a width of 4800 km the trench develops a 'W'-shaped curvature and slab morphology varies along-strike (see Figures 8 and

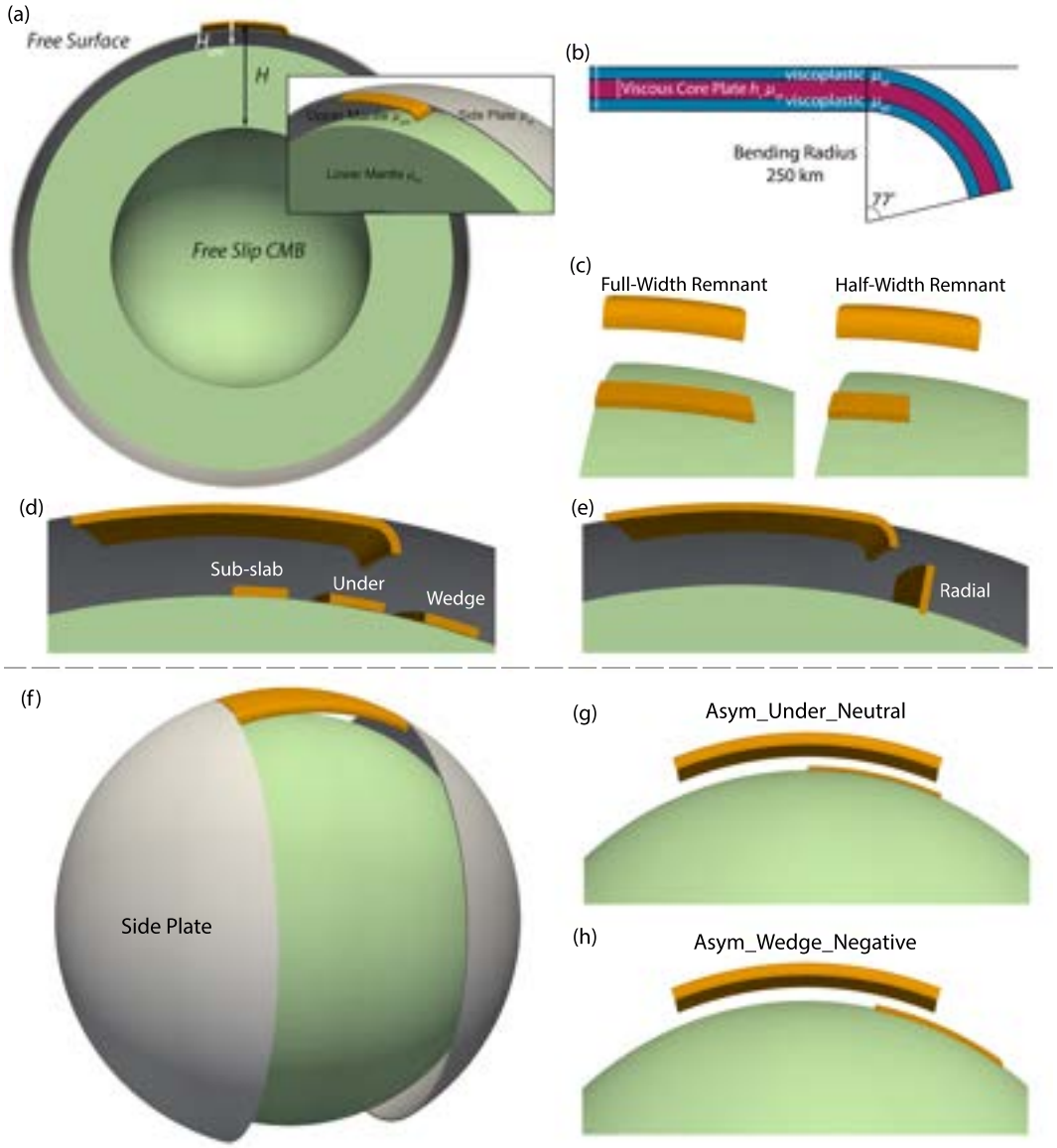

Figure 2. Simulation setup for (a–e) symmetric cases modelled in a hemispherical shell domain and (f–h) asymmetric cases modelled in a full spherical shell domain: (a) Hemispherical shell domain setup, where the domain is bounded by the symmetry plane of the system, whilst bottom and top (inner and outer) boundaries approximate Earth's core-mantle-boundary and surface, respectively; (b) Initial slab tip geometry of our layered visco-plastic plates; (c) Front view of full-width and half-width remnant configurations with respect to the width of the subducting plate; (d) Side view of positions of horizontally oriented remnants, in the sub-slab region, under the initial trench location, and in the mantle wedge region; (e) Side view of the configuration of a radially oriented remnant; (f) Spherical shell domain setup, with two side plates covering the domain adjacent to the subducting plate; (g) Front view of remnant location in case Asym_Under_Neutral; (h) Front view of remnant location in case Asym_Wedge_Negative.

246 10 in Section 3 below). For horizontal remnants, the majority of the cases have an ini-

Table 2. Simulations examined and associated parameter values. w = slab width; w_{rem} = remnant width; D_{rem} =remnant depth; $\Delta\rho_{\text{rem}}$ =density contrast between remnant and ambient mantle.

Case	w (km)	w_{rem} (km)	Orientation	D_{rem} (km)	Position	$\Delta\rho_{\text{rem}}$ (kg m^{-3})
Symmetric						
W2400	2400	N/A	N/A	N/A	N/A	N/A
W2400_Neutral	2400	2400	Horizontal	660	Wedge	0
W2400_Wedge	2400	2400	Horizontal	660	Wedge	80
W2400_Subslab	2400	2400	Horizontal	660	Sub-slab	80
W2400_Under	2400	2400	Horizontal	660	Under	80
W2400_Under_1000	2400	2400	Horizontal	1000	Under	80
W2400_Radial	2400	2400	Radial	700	Wedge	80
W2400_Wedge_half	2400	1200	Horizontal	660	Wedge	80
W2400_Subslab_half	2400	1200	Horizontal	660	Sub-slab	80
W4800	4800	N/A	N/A	N/A	N/A	N/A
W4800_Wedge	4800	4800	Horizontal	660	Wedge	80
W4800_Subslab	4800	4800	Horizontal	660	Sub-slab	80
W4800_Under	4800	4800	Horizontal	660	Under	80
W4800_Wedge_half	4800	2400	Horizontal	660	Wedge	80
W4800_Subslab_half	4800	2400	Horizontal	660	Subslab	80
Asymmetric						
Asym_Under_Neutral	4800	2400	Horizontal	660	Under	0
Asym_Wedge_Negative	4800	2400	Horizontal	660	Wedge	80

tial remnant depth of 660 km, sitting on the mantle transition zone where slab stagnation is commonly observed (e.g., Gorbatov et al., 2000; Fukao et al., 2009; van der Meer et al., 2018; Wu & Suppe, 2018). An additional case with a remnant depth of 1000 km is also examined to investigate the effect of deeper remnants (e.g., Fukao & Obayashi, 2013; Zahirovic et al., 2014; van der Meer et al., 2018; Braszus et al., 2021). The radially oriented remnant is placed between 300 and 700 km depth, in close proximity with the slab. While most remnants have the same density contrast with ambient mantle as our subducting plates, we have also simulated a neutrally buoyant remnant to investigate the effect of a purely viscous anomaly. All cases, and their associated parameter values, are listed in Table 2.

As Earth's subduction systems and their interactions with remnant slabs are rarely symmetric, we design two additional asymmetric cases that utilise the full spherical shell domain and illustrate the complexity of slab-remnant interactions under these scenarios. Case *Asym_Under_Neutral* has a neutral horizontally-oriented remnant at 660 km depth, beneath the initial trench location under half of the 4800 km wide subducting plate, as illustrated in Figure 2(g). Case *Asym_Wedge_Negative* has a negatively buoyant remnant of 2400 km width in the wedge location, with the centre of the remnant aligned to the edge of the 4800 km wide subducting plate, and thus extending beyond the slab edge (Figure 2h). While a more complete and systematic examination of different combinations of remnant properties and locations is required to fully quantify the impact of remnants on subduction zones, due to the computational costs of our simulations, we focus on two demonstrative asymmetric cases. Nonetheless, these cases show how the asymmetric interaction between slabs and remnants alters the subduction process, providing a basis for future studies.

We calculate several diagnostic outputs to quantify slab-remnant interactions. When doing so, the boundary of the slab is defined by the 0.5 contour of the plate material volume fraction (material volume fraction = 1 when the material is plate, 0 otherwise). Based on this contour, we extract the slab tip depth, the trench location and the trailing edge position, as well as rates of slab descent, trench retreat and plate advance. We calculate the average slab dip in the upper mantle from the surface to 650 km depth by approximating the geometry of the slab to be linear and comparing the difference in lateral positions over this depth range, with respect to the direction of gravity at the slab centre at 325 km depth. Similarly, remnant depth and velocity are extracted using the 0.5 contour of the remnant material volume fraction. The angular distance between slab and remnant is defined as the minimum difference in longitude between the deepest point of the remnant and the portion of the downgoing plate that is below 250 km depth. Measurements are taken at the symmetry plane unless otherwise specified. We also trace the evolution of trench geometry relative to the initial trench shape.

3 Results

In the following sections we first investigate the role of remnant density by comparing cases W2400_Neutral and W2400_Wedge with their W2400 reference case. Next, we explore the influence of different remnant locations and orientations, before examining the effect of remnant size on narrow (2400 km) and wide (4800 km) subduction zones with a focus on the evolution of trench shape. With a general understanding of how remnant properties influence the evolution of subducting systems from symmetric cases, we evaluate two asymmetrical cases with different remnant location and density, highlighting some of the main effects that remnants can have on subduction dynamics.

3.1 Role of Remnant Density

The reference case, W2400, has a plate width that is close to Earth's mean trench length at the present day (e.g. Heuret et al., 2007; Müller et al., 2016; F. Chen et al., 2022b). At this width, the slab remains reasonably uniform in its along-strike morphology as it descends, with its temporal evolution and corresponding cross-sectional flow field at the symmetry plane displayed in Figure 3(a). During the initial phase of subduction, the slab tip steepens, and two poloidal flow cells develop in the mantle wedge and sub-slab regions, over a distance similar to the depth of the upper mantle and length of the slab (as in Piromallo et al. (2006)). These poloidal cells flow from regions of high pressure towards regions of low pressure, as illustrated in Figure 4(a). During the upper mantle sinking phase, the trench retreats steadily and accounts for $\sim 30\%$ of total subduction, with the remainder accommodated via trailing edge advance (Figure 5b,c,d). Following interaction with the viscosity jump at 660 km depth, flow velocities in the wedge poloidal cell diminish as the slab tip deflects and sinks into the more viscous lower mantle (Figure 3a). At the same time, mantle material flows across the transition zone into the lower mantle, into a higher pressure region beneath the slab tip (Figure 4a). At this point, the slab sinking rate reduces from its free upper-mantle Stokes velocity of ~ 9 cm/yr to a substantially lower velocity of ~ 3 cm/yr (Figure 5a,e), as the upper mantle portion of the slab steepens and develops buckling folds (Figure 3a, 5f).

When a neutrally buoyant remnant is placed in the wedge region at 660 km depth (case W2400_Neutral, red dashed line in Figure 5), we find that slab tip depth, trailing edge advance, slab sinking rate and upper mantle dip angle diagnostics are similar to the W2400 case (Figure 5a,c,e,f). W2400_Neutral displays a slightly increased trench retreat velocity (Figure 5b,d), which is also evident from the increased velocity amplitude of the sub-slab poloidal flow cell (Figure 3a,b). Upon slab transition-zone interaction, the viscous remnant in front of the slab tip hinders slab tip advance, leading to more retreat as the slab adjusts to maintain its sinking rate (Figure 5b), resulting in a shorter deflected

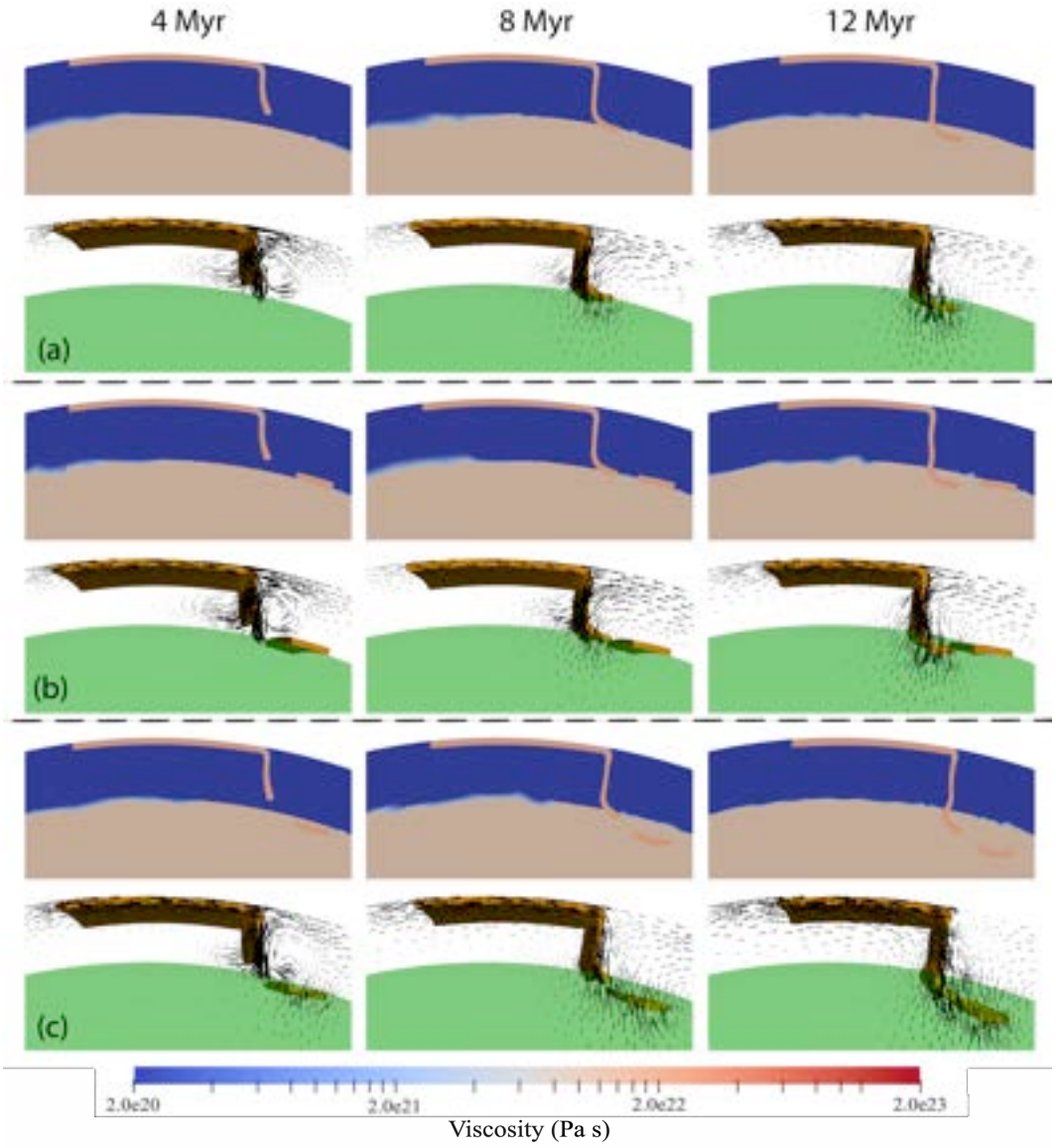

Figure 3. Snapshots illustrating the spatio-temporal evolution of slab morphology through the viscosity field (top), and poloidal flow cells in the mantle wedge and sub-slab regions (bottom) at simulation times of 4 8 and 12 Myr for cases: (a) W2400; (b) W2400_Neutral; and (c) W2400_Wedge, respectively. The largest arrow in the bottom panels represents a velocity magnitude of 9.6 cm/yr.

slab tip. The neutrally buoyant remnant remains close to its initial location until it is pulled into the lower mantle and towards the subducting slab via slab induced flow (Figure 5g,h,i), initially sinking at the side closest to the subducting plate (Figure 3b). Despite these subtle differences in the flow regime, the pressure field in the case with a neutrally buoyant remnant is similar to the reference case (Figure 4b).

Case W2400_Wedge (continuous red line in Figure 5) illustrates the effect of a negatively buoyant remnant in the mantle wedge region above the transition zone. The remnant's negative buoyancy drives downwelling flow, leaving in its wake a low pressure re-

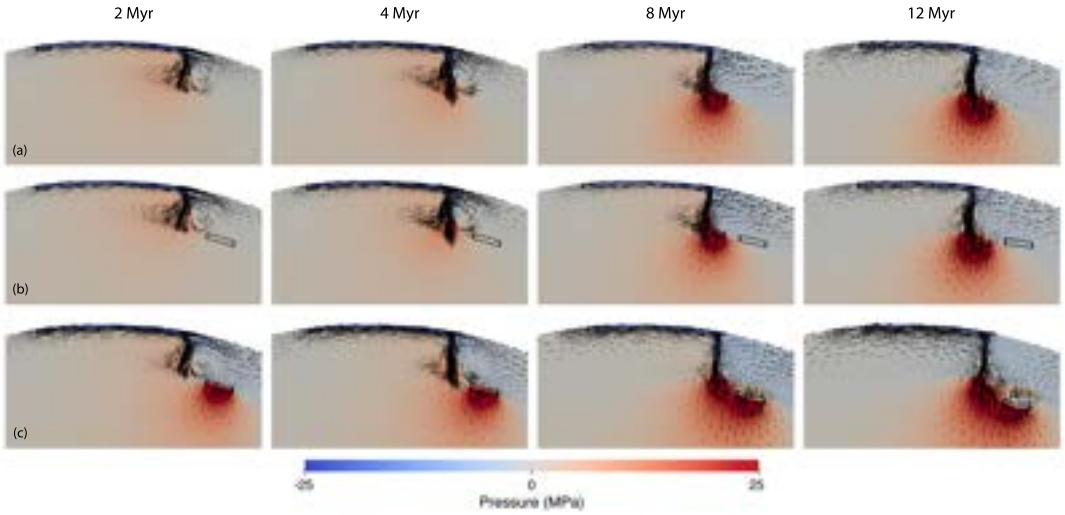

Figure 4. Evolution of pressure field at the symmetry plane at simulation times of 2, 4, 8 and 12 Myr, respectively, for cases: (a) W2400; (b) W2400_Neutral; and (c) W2400_Wedge. Arrows indicate the direction and magnitude of velocity up to 9.6 cm/yr.

gion of similar size and strength (Figure 4c) as that of the slab once it penetrates into the lower mantle (Figure 4a). The slab is pulled towards this low pressure area, increasing the slab descent velocity and trailing edge advance rate relative to the reference case (Figure 5a,c,e), and forcing the slab into an advancing regime (negative trench retreat) with a steep upper mantle dip angle (Figure 5b,d,f). Remnant induced downwelling pulls material across the MTZ long before the arrival of slab material at 660 km depth, which differs from the two previous cases analysed (Figure 4c), whilst also modifying the mantle wedge and sub-slab poloidal flow cells (Figure 3c). The remnant's initial sinking velocity is similar in magnitude as that of the slab once it enters the lower mantle, as expected from the similar size and density contrast of the slab and remnant. Over the duration of our simulation, the remnants' sinking velocity increases from 3 to 3.5 cm/yr. Beyond the initial phase of subduction, the angular distance between the plate and remnant decreases over time, increasingly aligning the flow fields induced by the slab and remnant (Figure 5h,i).

These cases demonstrate some of the impacts of remnants on the evolution of subduction systems. Even in the absence of buoyancy anomalies, highly viscous material can modulate the flow regime, altering the dynamics and morphology of adjacent descending slabs. Negatively buoyant remnants drive downward flow, aiding the descent of adjacent downgoing slabs. At the same time, slabs aid the descent of remnants. Over time, the remnant and slab move towards each other, resulting in an increase in velocity of both as the lateral distance between them reduces (Figure 5e,h,i).

3.2 Role of Remnant Location and Orientation

We next compare simulations where identical remnants (geometry, volume, density and viscosity) are placed in different positions with respect to case W2400, to investigate the effect of remnant location and orientation. Cases W2400_Wedge, W2400_Subslab and W2400_Under simulate horizontal remnants at varying lateral distances from the initial trench position, and at different positions within the asymmetric flow field set up behind and in front of the subducting slab. We compare cases W2400_Under and W2400_Under_1000

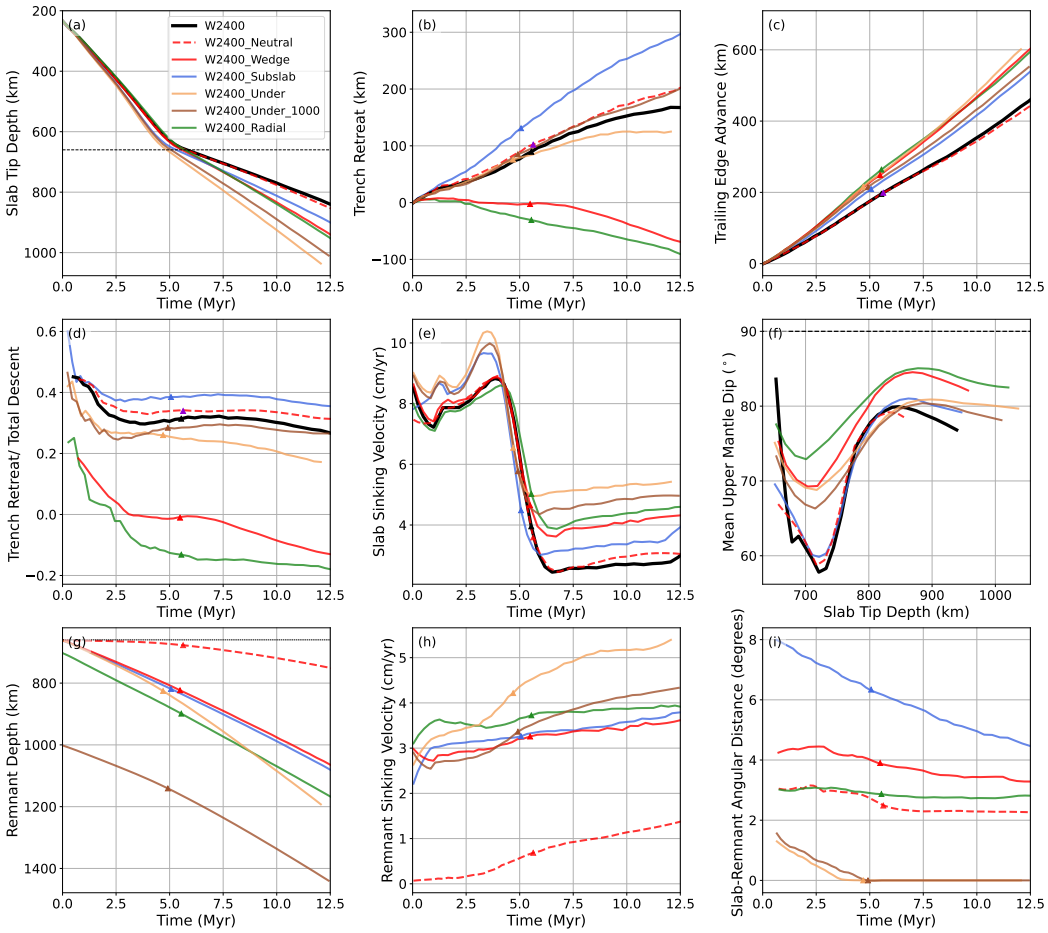

Figure 5. Comparisons between simulations of a 2400 km wide plate with 2400 km wide remnants with different properties, locations and orientations: (a) slab tip depth as a function of time, where the upper–lower mantle boundary is indicated by the black dotted line at 660 km depth; (b) amount of trench retreat; (c) amount of plate advance, measured at the plate's trailing edge; (d) ratio of trench retreat to total descent, which is the sum of trench retreat and trailing edge advance; (e) slab sinking velocity; (f) average slab dip in the upper mantle, with the black dashed line indicating a vertical slab with dip angle of 90°; (g) remnant depth; (h) remnant sinking velocity; and (i) the minimum angular distance between subducting slab tip and the deepest point of the remnant. Triangles indicate the time of first slab tip interaction with the viscosity jump at 660 km depth. All measurements are taken at the symmetry plane.

to investigate how the depth of the remnant modulates its influence on the subducting slab. Comparisons between cases W2400_Wedge (horizontally oriented remnant) and W2400_Radial (radially oriented remnant) highlight how remnant orientation influences interaction with adjacent subducting systems. Remnants of similar mass and shape should set up similar Stokes–sinking mantle flow fields around them, but radially oriented remnants would be expected to experience somewhat lower drag than horizontally oriented remnants in the gravity driven flow.

Case W2400_Subslab, where the negatively buoyant remnant is placed in the subslab region above the transition zone, displays the greatest rate of trench retreat across

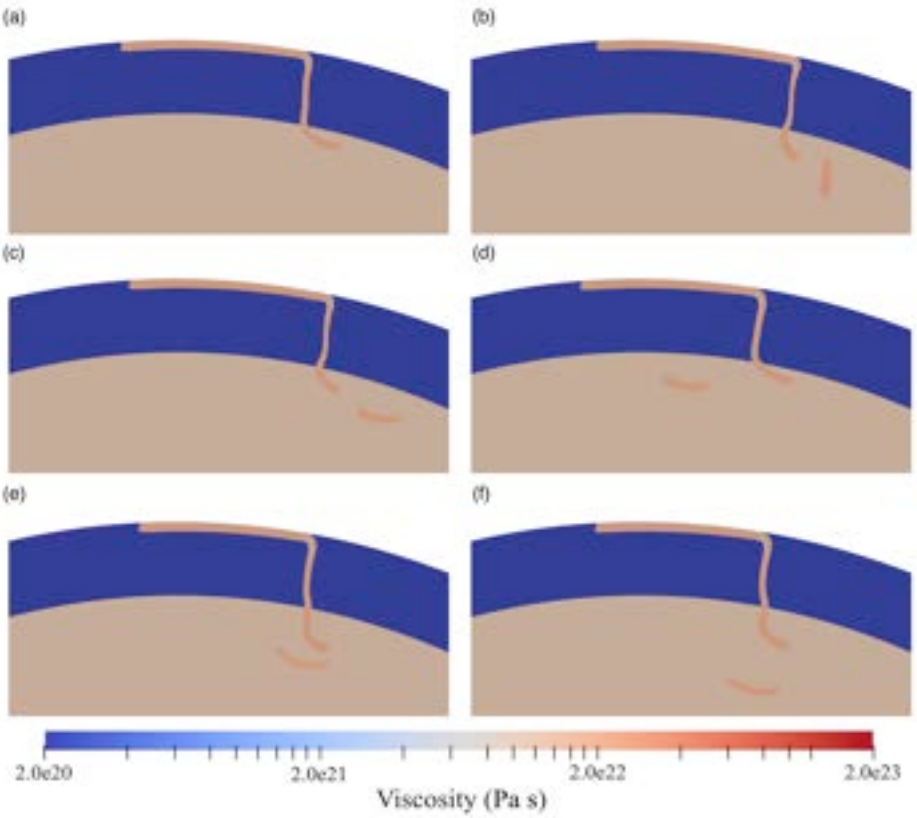

Figure 6. Slab morphology, illustrated by the viscosity field at the symmetric mid-plane at 12 Myr, for cases with 2400 km-wide plates with equally wide remnants: (a) W2400 (reference case); (b) W2400_Radial; (c) W2400_Wedge; (d) W2400_Subslab; (e) W2400_Under; and (f) W2400_Under_1000.

all 2400 km wide simulations considered, accounting for $\sim 40\%$ of total subduction (Figure 5b,d). The upper mantle portion of the slab has a shallower dip angle than the reference case and displays minimal vertical folding (Figures 5f and 6d). Although the remnant sinks at a velocity close to the remnant of case W2400_Wedge (Figure 5g,h), the slab displays the slowest sinking and trailing edge advance velocities of all 2400-km wide cases considered with negatively buoyant remnants (Figure 5a,c,e). The remnants in cases W2400_Subslab and W2400_Wedge are equidistant from the initial trench location, but in case W2400_Subslab it is further away from the slab tip (Figure 5i). Nonetheless, the remnant is able to pull the slab laterally, evidenced through enhanced trench retreat rates (towards the remnant) and a reduced angular distance of $\sim 4^\circ$ between remnant and slab (Figure 5i).

A negatively buoyant remnant is placed directly below the initial trench location in case W2400_Under. In this scenario, we observe the fastest sinking velocities for both the subducting plate and the remnant across all 2400-km cases cases considered (Figure 5a,e,g,h) as the mantle flow fields set up by the slab and remnant most effectively enhance each other. Trench retreat is reduced relative to the reference case, but trailing edge advance is the largest of all cases considered, accounting for more than 80% of total subduction (Figure 5b,c,d). The slab has a steep angle (greater than 69° throughout the simulation, Figure 5f) and, as a result, slab tip deflection at the transition zone is reduced (Figure 6e). The angular distance between the slab tip and the remnant re-

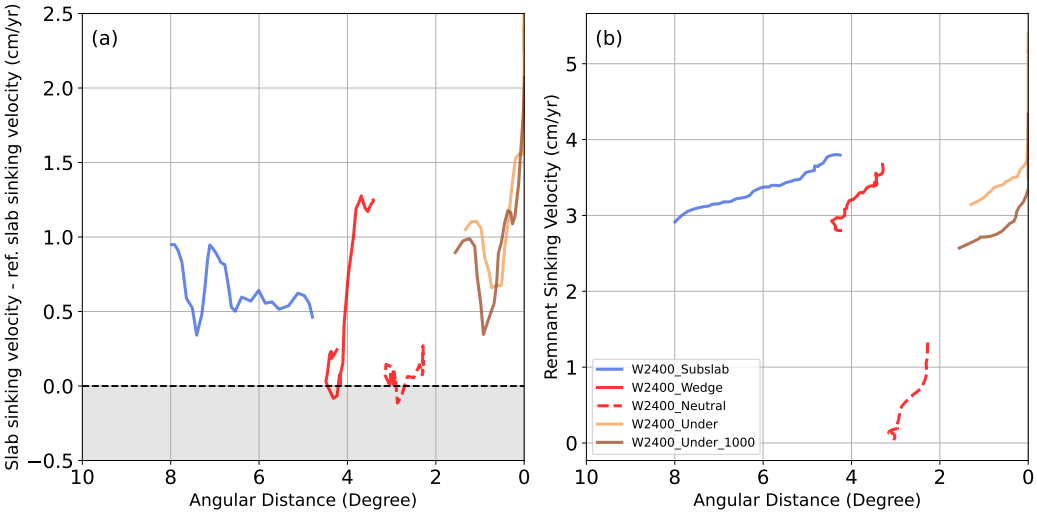

Figure 7. Comparisons of: (a) differences in sinking velocity relative to the reference W2400 case (measured when the slab tip is at the same depth) – values above 0 indicate that the presence of the remnant increases slab sinking velocities; (b) remnant sinking velocities, as a function of angular distance between remnant and slab tip.

duces initially, as the slab tip rotates towards the remnant; once their angular distance is 0° (i.e., the descending slab is radially above the deepest point of remnant), the slab and remnant move in the same radial direction. We note that when the remnant is placed deeper, 1000 km below the trench (case W2400_Under_1000), its influence on the slab is reduced, although general trends for each diagnostic are similar to Case W2400_Under.

In case W2400_Radial, the remnant is oriented radially in the mantle wedge between 300 and 700 km depth, 500 km away from the initial trench position. The orientation and location of the remnant in closer proximity to the descending slab and a somewhat stronger remnant flow field drive an increase in trench advance and the slab's upper mantle dip angle compared with the W2400_Wedge case. Indeed, of all 2400-km wide cases considered, this displays the most trench advance and the steepest upper mantle slab dip angle (Figure 5b,d,f), albeit with a similar slab sinking velocity and plate advance velocity to its horizontal counterpart, W2400_Wedge (Figure 5a,c,e). The angular distance between the slab and remnant remains stable after slab transition zone interaction, whereas in the horizontal W2400 Wedge case, the angular distance continues to reduce (Figure 5i). At this stage of model evolution, the radial remnant and slab are descending in their respective radial directions towards the centre of the sphere, hence there is no longer any effective lateral flow pulling them towards each other (Figure 6b). Horizontal remnants in W2400_Wedge and W2400_Subslab cases rotate towards the descending slab so that their angular distances reduce while the slab also moves towards the remnant either through advance or retreat.

The distance between the remnant and the subducting slab plays an important role in determining remnant impact on the subduction process. As shown in Figure 7(a), negatively buoyant remnants can increase slab sinking velocities even when displaced horizontally ~ 1000 km from the slab tip, with an increase in sinking velocity of ~ 0.5 to ~ 1.0 cm/yr relative to the reference case in Case W2400_Subslab, at an angular distance of 8°. Cases W2400_Wedge, W2400_Under and W2400_Under_1000 demonstrate that the increase in slab sinking velocity relative to the reference case is proportional to

the proximity of a negatively buoyant remnant, with relative sinking velocities generally increasing as the slab-remnant distance decreases, as slab and remnant flow fields align more closely. Where distances between the remnant and slab are less than 100-200 km, sinking velocities can be enhanced by up to a factor of 2 (see also Figure 5e). A comparable effect is also measured for the remnant, as shown in Figure 7(b), where all remnants exhibit higher sinking velocities as they approach the subducting slab.

These cases demonstrate that, for a given buoyancy anomaly, the proximity of a remnant to a subducting slab (both laterally and radially) controls its ability to accelerate slab descent. Furthermore, more energy is expended on horizontal transportation and/or rotation of the downgoing slab when the lateral distance between remnant and slab increases. If the remnant is located in front of a subducting slab, the slab tends to advance and steepen, but if the remnant is located behind the subducting slab, beneath the downgoing plate, the trench retreats to reduce the distance between slab and remnant. Downgoing flow from the descending slab also rotates horizontal remnants towards the slab, reducing the angular distance between them. These motions lead to increasing alignment of the flow set up by the slab and remnant. As a result, when the remnant and slab are oriented radially in the direction of gravity, further rotations or lateral movements are minimal, with their angular distance unchanged for the remainder of their descent.

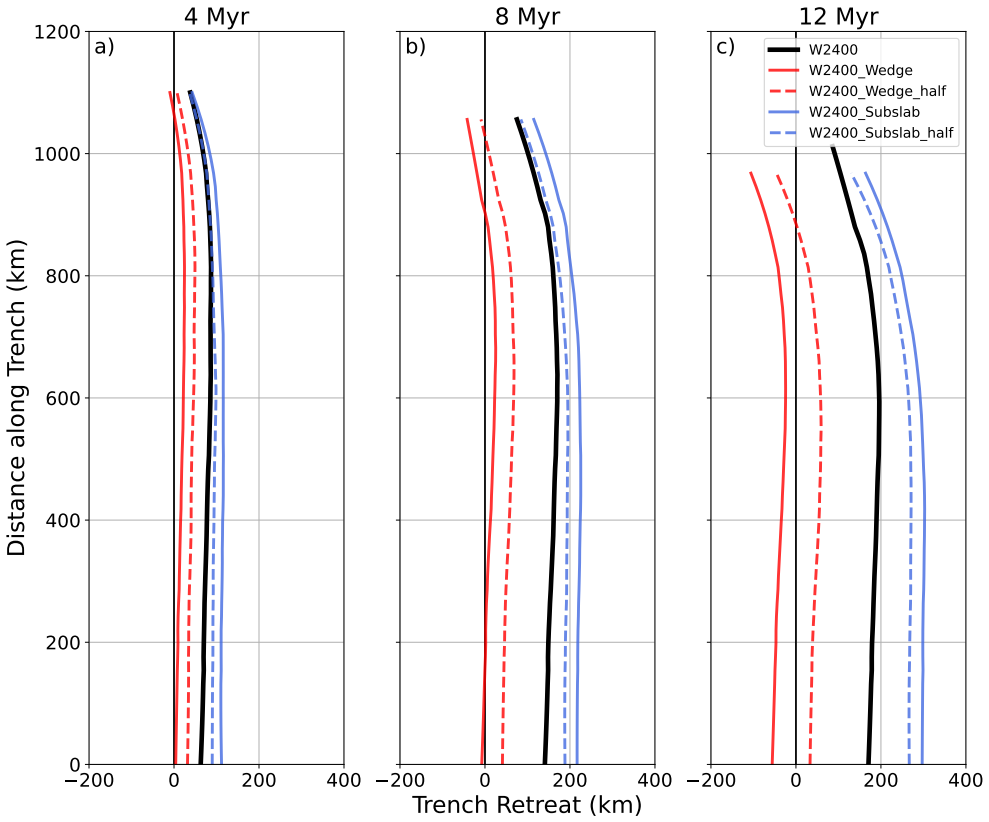

Figure 8. Spatio-temporal evolution of trench locations for cases W2400, W2400_Wedge, W2400_Wedge_half, W2400_Subslab, W2400_Subslab_half at simulation times of: (a) 4 Myr; (b) 8 Myr; and (c) 12 Myr.

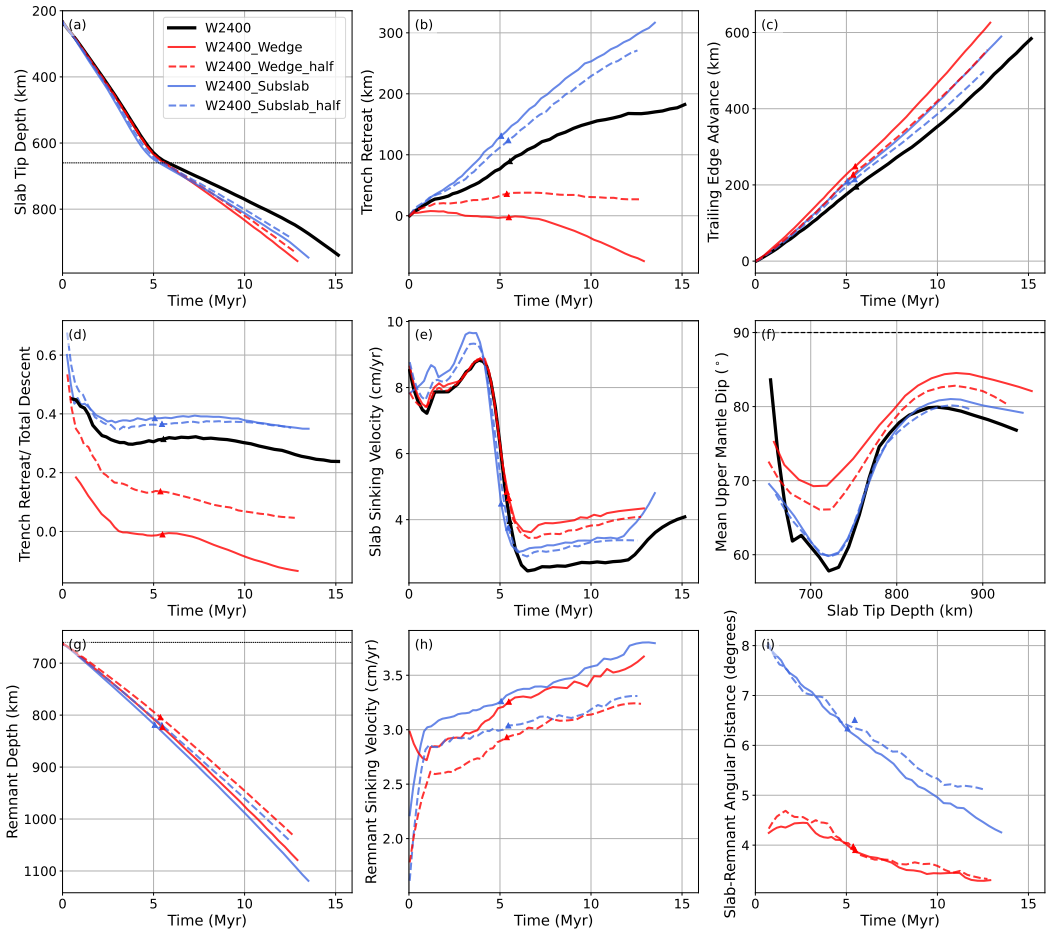

Figure 9. Comparisons between simulations of a 2400 km wide plate with remnants of different widths and positions: (a) slab tip depth as a function of time, where the upper–lower mantle boundary is indicated by the black dotted line at 660 km depth; (b) amount of trench retreat; (c) amount of plate advance, measured at the plate's trailing edge; (d) ratio of trench retreat to total descent, which is the sum of trench retreat and trailing edge advance; (e) slab sinking velocity; (f) average slab dip in the upper mantle, with the black dashed line indicating a vertical slab with dip angle of 90°; (g) remnant depth; (h) remnant sinking velocity; and (i) the minimum angular distance between subducting slab tip and the deepest point of the remnant. Triangles indicate the time of first slab tip transition-zone interaction. All measurements are taken at the symmetry plane.

3.3 Role of Remnant Size and Slab Width

Subduction zones develop curvatures at their edges due to toroidal flow around the slab. The evolution of trench shape depends on plate age and width: narrow plates tend to develop 'C'-shaped trenches, where the trench retreats most at the centre, while wider plates tend towards developing 'W'-shaped curvatures, where trench retreat is lower at the centre and the edges of the slab (e.g., Schellart et al., 2007; F. Chen et al., 2022b). Here, we examine the influence of remnants for cases with plate widths of 2400 and 4800 km, which develop 'C' and 'W'-shaped trenches in their reference cases, respectively (W2400 and W4800: Figures 8 and 10).

3.3.1 Influence on 2400-km wide slabs

Our previous work demonstrates that trenches consistently develop an elongated 'C'-shape for 2400 km wide slabs (F. Chen et al., 2022b). In cases W2400_Wedge and W2400_Subslab, the addition of a full-width remnant does not modify predicted 'C'-shaped trench curvature (Figure 8), despite influencing trench motions, as discussed in Section 3.2.

To examine the influence of smaller remnants, we investigate two additional cases with remnant widths that are half of the plate width, positioned beneath the centre of the trench. The half-width remnant in Case W2400_Wedge_half has a lower sinking velocity (maximum of ~ 3.2 cm/yr) than its full-width remnant counterpart (maximum of ~ 3.6 cm/yr – Figure 9h) and, hence, drives less of an increase in slab descent velocity. As a result, relative to its full-width equivalent, the slab sinks slower with less trailing edge advance, at a shallower dip angle (Figure 9a,c,f). The half-width remnant is also less able to pull the slab towards it. As a result, despite significantly reduced trench retreat rates compared to case W2400, the trench remains in a retreating regime, rather than entering the advancing regime of case W2400_Wedge (Figure 9b,d). While the angular distance between the half-width remnant and the centre of the plate reduces (Figure 9i), no significant curvature develops along the trench (Figure 8).

The half-width remnant in Case W2400_Subslab_half drives a similar response to Case W2400_Wedge_half, with its influence on the subducting plate less than its corresponding full-width case, W2400_Subslab. Due to the lower remnant sinking velocity (maximum of ~ 3.3 cm/yr versus ~ 3.9 cm/yr in W2400_Subslab), the slab in W2400_Subslab_half sinks slower, whilst trench retreat and trailing edge advance also reduce (Figure 9), with a negligible influence on trench curvature.

Thus, smaller remnants have less of an influence on the descending slab than full-width remnants. This is in line with expectations from their Stokes sinking velocities (Eq. 1). On 2400-km wide cases that tend to develop 'C'-shaped trenches, such remnants are unable to generate sufficient pull to overcome the bending resistance of the subducting plate, with trench shape remaining similar to corresponding reference cases.

3.3.2 Influence on 4800-km wide slabs

At a plate width of 4800 km, the reference case (W4800) develops a 'W'-shaped trench ('S'-shaped in the halved domain, Figure 10) with the centre of the trench stagnating at its initial location. In this section, we examine the effects of full-width remnants via cases W4800_Under, W4800_Wedge, and W4800_Subslab; and half-width remnants via cases W4800_Wedge_half and W4800_Subslab_half.

Similar to case W2400_Under, where the remnant is placed directly beneath the trench, case W4800_Under also displays the fastest descent velocities for both the subducting slab and the remnant over all 4800 km wide cases considered (Figure 11a,e,g,h). As in its 2400 km wide equivalent, this case displays elevated trailing edge advance and a steeper upper mantle dip angle compared to its reference case (Figure 11c,f). The trench advances from its initial location (Figure 11b), with the 'W'-shaped curvature less prominent compared to the reference case (Figure 10, Figure 12a,b).

The full-width remnant in case W4800_Wedge drives significant trench advance and steepening of the subducting slab (Figure 11b,d,f). Trench curvature is reduced relative to the reference case (Figure 10), and slab morphology becomes more uniform along strike (Figure 12c). The half-width remnant (case W4800_Wedge_half) is less able to drive trench advance at the symmetry plane (Figure 11b,d). However, as this anomaly is placed below the stagnating region of the trench, it enhances the contrast in trench curvature be-

tween the advancing centre and the retreating edges of the slab (Figure 10), driving substantial along-strike variations in slab morphology (Figure 12d).

Sub-slab remnants in cases W4800_Subslab and W4800_Subslab_half increase trench retreat while reducing the upper mantle slab dip angle (Figure 11b,d,f). On the symmetry plane, full-width and half-width remnants have similar effects on slab dynamics, except that the angular distance between the slab and remnant reduces more for the full-width remnant. The full-width remnant reduces 'W'-shaped trench curvature, but not to the same extent as the half-width remnant, which almost generates an elongated 'C'-shaped trench with a straight centre (Figure 10). The localised retreat-driving flow induced by the half-width sub-slab remnant counteracts the subducting plate's natural tendency to stagnate at the centre, limiting along-strike variations in trench retreat velocity.

In summary, the trench shape of wider subduction systems are more strongly influenced by remnants than narrower plates. Because of the larger width, the effect of toroidal flow around the slab is limited to regions within 1000-1500 km from the slab edges. When additional descent-driving forces act uniformly along strike, the relative impact of toroidal flow at the edge reduces, resulting in less trench curvature. When a half-width remnant drives the slab centre to retreat, counteracting the natural tendency of the trench to stagnate, the trench remains relatively straight. Conversely, when the half-width remnant acts to enhance slab stagnation at the centre, the trench is able to develop increased cur-

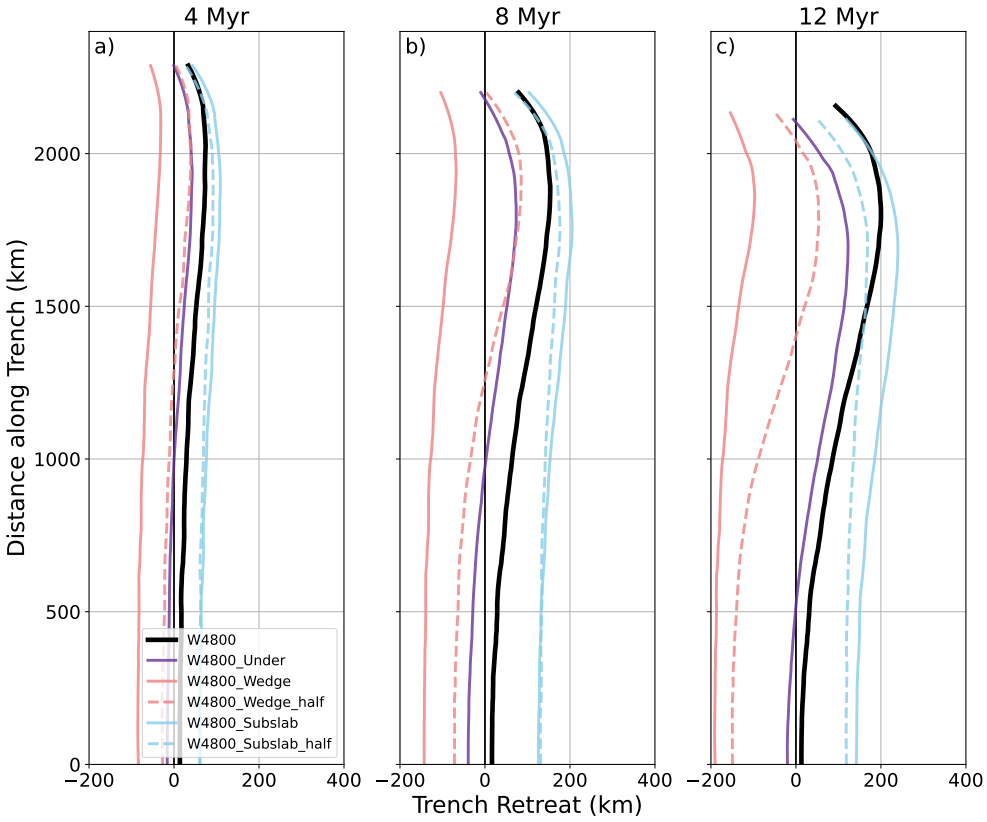

Figure 10. Spatio-temporal evolution of trench locations for cases W4800, W4800_Under, W4800_Wedge, W4800_Wedge_half, W4800_Subslab, and W4800_Subslab_half at simulation times of (a) 4 Myr, (b) 8 Myr, and (c) 12 Myr.

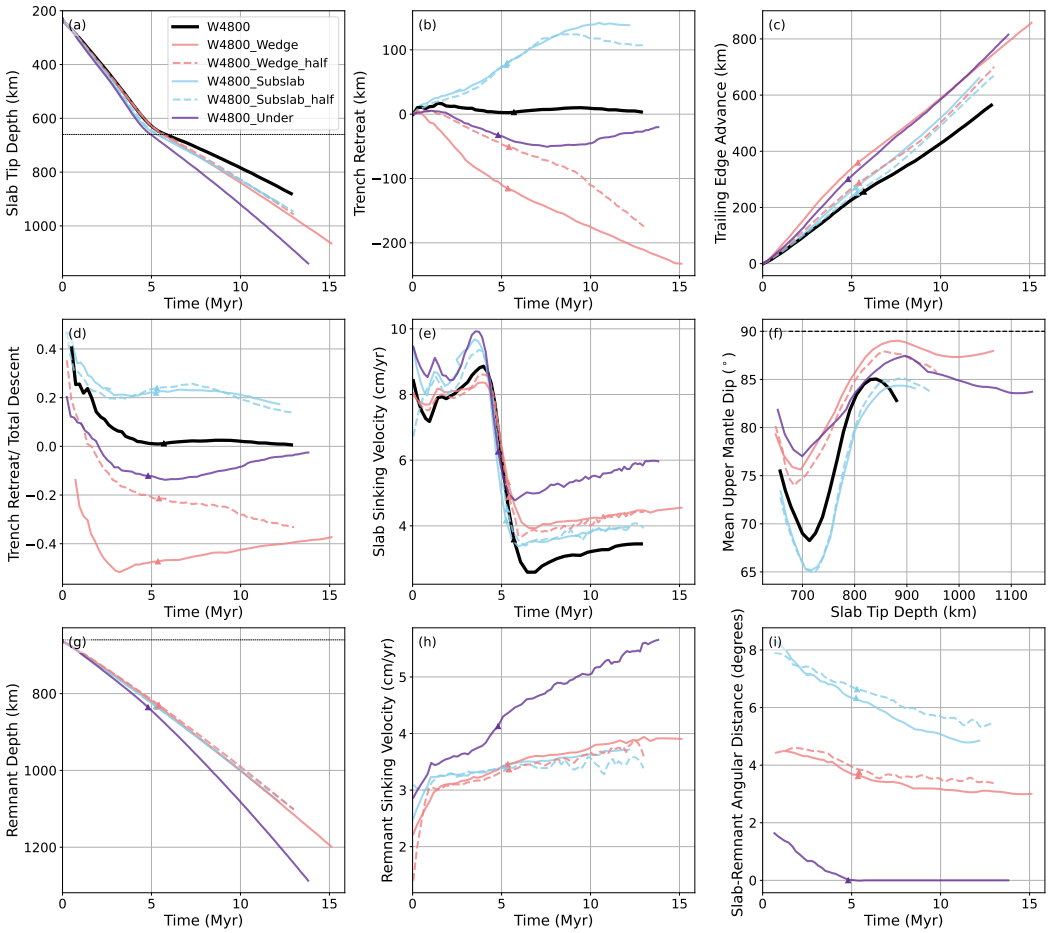

Figure 11. Comparisons between simulations of a 4800 km wide plate with remnants of different widths and positions: (a) slab tip depth as a function of time, where the upper–lower mantle boundary is indicated by the black dotted line at 660 km depth; (b) amount of trench retreat; (c) amount of plate advance, measured at the plate's trailing edge; (d) ratio of trench retreat to total descent, which is the sum of trench retreat and trailing edge advance; (e) slab sinking velocity; (f) average slab dip in the upper mantle, with the black dashed line indicating a vertical slab with dip angle of 90°; (g) remnant depth; (h) remnant sinking velocity; and (i) the minimum angular distance between subducting slab tip and the deepest point of the remnant.Triangles indicate the time of first slab tip transition-zone interaction. All measurements are taken at the symmetry plane.

vature. For narrower plates, these different driving forces act in close proximity along the trench, and are typically unable to overcome the plate bending resistance and, hence, these slabs remain in a 'C'-shape, regardless of remnant size and location.

3.4 Asymmetric Remnants

While the hemispherical cases allow us to systematically explore how remnants with different properties interact with subducting slabs, the full spherical models considered in this section allow us to demonstrate asymmetric slab interactions with neutrally and negatively buoyant remnants via cases Asym_Under_Neutral and Asym_Wedge_Negative.

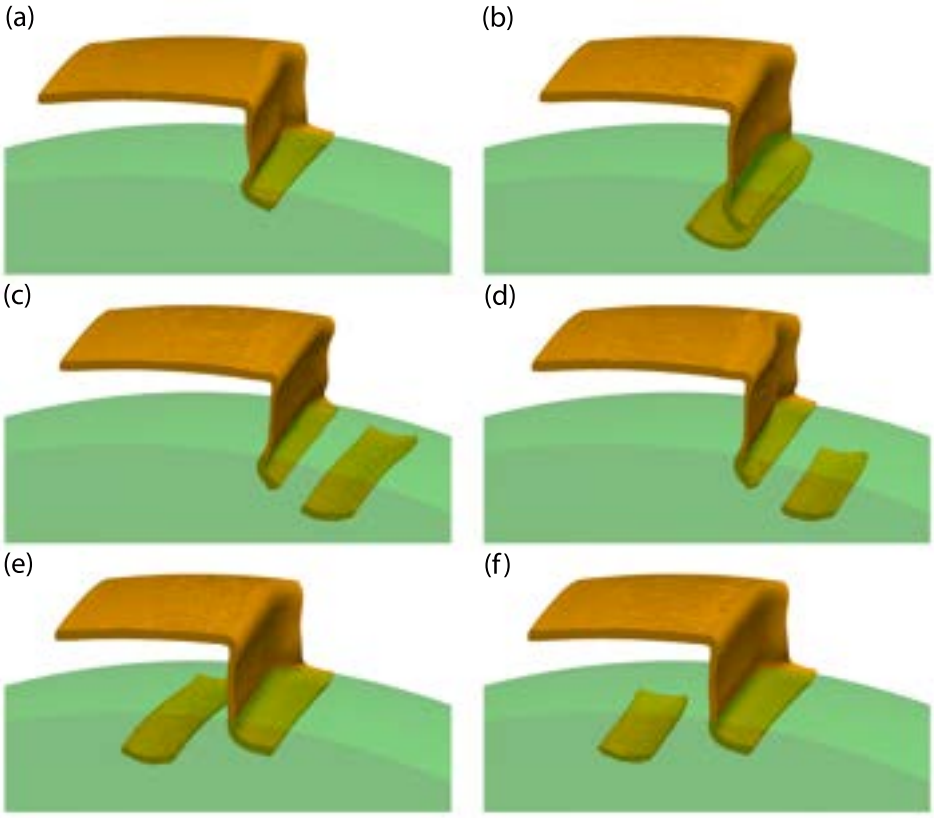

Figure 12. 3-D morphology of 4800 km wide plates at 12 Myr: (a) W4800 (reference case); (b) W4800_Under; (c) W2400_Wedge; (d) W2400_Wedge_half; (e) W2400_Subslab; and (f) W2400_Subslab_half.

Case Asym_Under_Neutral is designed to examine the effect of an active slab partially subducting on to a stagnant remnant at the transition zone, where the remnant is not actively sinking and driving mantle flow. Case Asym_Wedge_Negative allows us to illustrate a more dramatic influence of a remnant, where it actively drives a downwelling flow cell in front of the subduction zone segment that displays the most trench retreat in the corresponding reference case.

For Case Asym_Under_Neutral, where half of the subducting slab descends into a neutrally buoyant remnant, slab descent is reduced locally, as evidenced by the along-strike variations in slab tip depth illustrated in Figures 13(a) and 14(a,c): the remnant's high viscosity hinders slab sinking, with the slab deflecting and resting above the remnant. At the edge of the remnant, the slab tip's depth transitions to the same state as the case without a remnant, penetrating deeper. These variations drive small changes in trench morphology, with more bulging observed towards the trench centre, and the region of most advance/stagnation shifted towards the remnant side when compared to the reference case (Figure 13c).

In case Asym_Wedge_Negative, the negatively buoyant remnant drives an increase in slab sinking velocities (Figures 13b and 14b,d) and strongly enhances trench advance along the proximal segment of the slab (Figure 13c). This highlights the asymmetric response: not only is trench advance enhanced, but the location of most advance shifts from the centre of the subducting plate (as in case W4800) towards the remnant (Figure 13c),

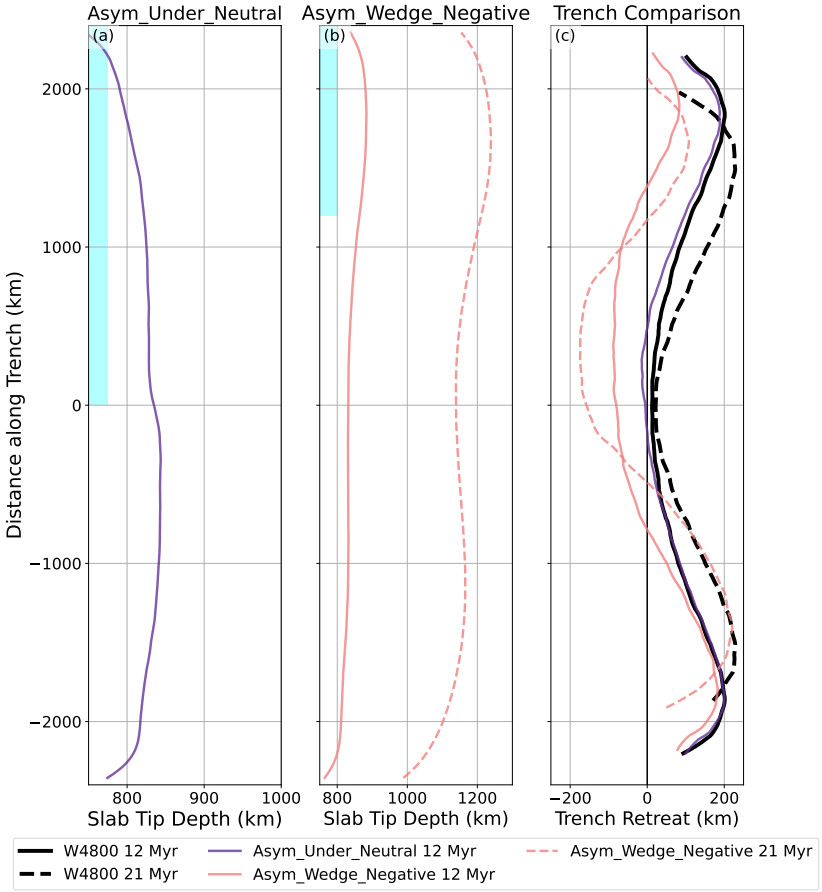

Figure 13. Along-strike variations of asymmetric spherical remnant models: (a) and (b) – variations in slab tip depth along the subducting slab for cases Asym_Under_Neutral and Asym_Wedge_Negative, respectively, at times of 12 Myr (solid lines) and 21 Myr (dashed lines). Distance along trench is defined as the distance from the symmetry plane in the direction parallel to the initial trench location. Blue boxes mark the initial trench section that is underlain by the remnant (they share the same latitude), note that the width of the remnant extends beyond the plotted region in (b); (c) trench shapes and the amount of retreat for cases W4800, Asym_Under_Neutral, and Asym_Wedge_Negative at 12 Myr and 21 Myr. Case W4800 was simulated in the hemispherical domain, thus for comparative purposes, the trench profile is mirrored at the symmetry plane.

illustrating the remnant's ability to alter trench shape and drive substantial along-strike variations in slab morphology (Figure 14e,f). To demonstrate how such a complex system evolves, we extended the simulation time of this case to 21 Myr: the system continues to develop more complex trench curvature and associated slab morphology as subduction evolves.

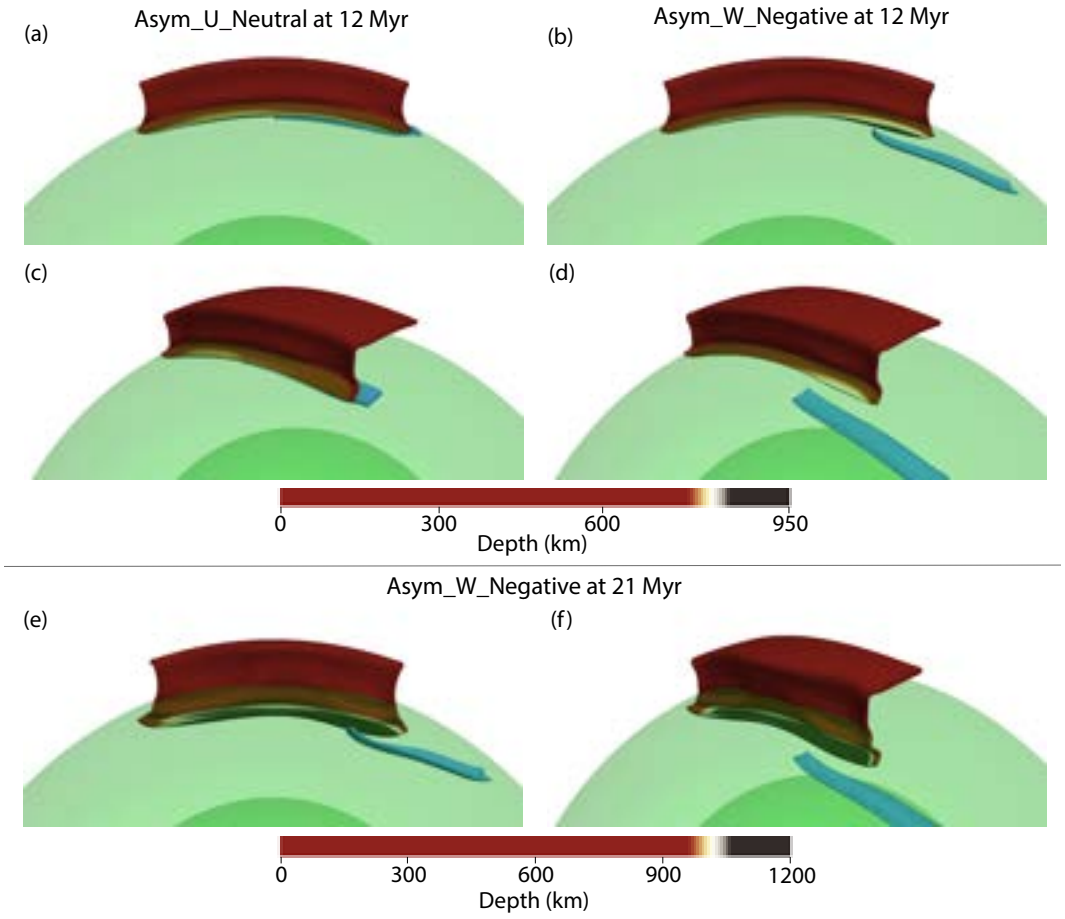

Figure 14. Slab and remnant morphology at 12 Myr for cases Asym_Under_Neutral (a,c) and Asym_Wedge_Negative (b,d), and at 21 Myr for the case Asym_Wedge_Negative (e,f) from different orientations. The subducting slabs are coloured by depth, with different colourbars used for at 12 Myr (a–d) and 21 Myr (e,f) to highlight variations in slab tip depth. The remnant is coloured in blue with the lower mantle in green.

4 Discussion

4.1 Applicability of Models

Our models are a simplified representation of Earth's subduction systems, but they provide fundamental insight into the first–order effects that slab remnants have on active subduction zones, and vice-versa. They are executed in a 3-D spherical shell domain, which is important for simulating Earth's subduction systems, particularly those that exceed 2400 km in width (F. Chen et al., 2022a). They also better capture the mechanical properties of subducting slabs than previous global models of mantle convection that incorporate slab remnants (e.g. Bunge et al., 2002; Yanagisawa et al., 2010; Lowman, 2011; Becker & Faccenna, 2011; D. R. Davies et al., 2012, 2015).

There are, however, simplifications of our model setup that may influence the evolution of slab morphologies and velocities. For example, the mantle transition zone is simulated solely as a viscosity jump that hampers flow into the lower mantle (e.g. Hager & Richards, 1989). We do not account for phase transitions, which will (temporarily)

further resist material transfer across this boundary (e.g., Ringwood, 1975; Ito & Yamada, 1982; Goes et al., 2017). Such a simplification may lead to our models predicting less transition–zone slab stagnation. Another limitation of our model set-up is the lack of an overriding plate, which will influence predicted trench migration rates and associated trench geometries and slab morphologies (e.g., Jarrard, 1986; Lallemand et al., 2005; Heuret et al., 2007; Capitanio, Stegman, et al., 2010; van Dinther et al., 2010; Garel et al., 2014). Finally, our model set-up lacks the evolution of the temperature field. The thermal structure of a subducting plate controls its thickness, density and rheology. While we use viscoplastic upper and lower layers of the subducting plate to mimic the deformation predicted by thermo-mechanical subduction models with non-linear temperature and stress dependent rheology, the diffusion of temperature and variations in thickness and buoyancy from ridge to trench are not captured in our simulations (e.g., OzBench et al., 2008; Stegman et al., 2010; Capitanio, 2013; Garel et al., 2014; Agrusta et al., 2017; F. Chen et al., 2022b). Furthermore, on Earth, the rheology of slabs and remnants changes with temperature, such that remnants at depth could become less plate-like than those considered herein (e.g., van Hunen et al., 2001; Andrews & Billen, 2009; Stadler et al., 2010). Nonetheless, assuming a thermal diffusivity of 1.0×10^{-6} $\mathrm{m^2\,s^{-1}}$, the time it takes for a 70 km thick slab to cool substantially would be $\sim$ 40 Myr. At an upper mantle sinking speed of 5-10 cm/yr, a slab crosses the upper mantle in 6-12 Myrs and thus retains most of its rheological contrast with background mantle. Buoyancy is modified even less, because while the thermal signature diffuses as the slab sinks, the integrated negative buoyancy only decreases if parts of the slab are sufficiently weakened that they can be eroded or removed by flow. Consequently, over the depth and time range investigated here, the impact of thermal diffusion on slab-remnant interaction will be secondary to the effects of density and strength contrasts that our models capture (e.g., Jarvis & Lowman, 2007; Kundu & Santosh, 2011; Quéré et al., 2013). We are therefore confident that our chosen model design, alongside the systematic comparisons across our model cases, isolates how different remnant properties (e.g., density, size, location) influence slab dynamics.

4.2 Potential Influences of Remnants on Subduction Zones

Based on the importance of slab pull for driving surface plate motions (e.g., Forsyth & Uyeda, 1975; Lithgow-Bertelloni & Richards, 1998; Becker & O'Connell, 2001), alongside the fact that regional subduction models predict an important role for incoming plate age and strength in dictating the dynamics of subduction (e.g., Bellahsen et al., 2005; Stegman et al., 2010; Garel et al., 2014; Suchoy et al., 2021), many studies have examined the correlations between different subduction parameters (e.g., Cruciani et al., 2005; Heuret & Lallemand, 2005; Lallemand et al., 2005; Doglioni et al., 2007; Vérard et al., 2015; Verard, 2019) in an attempt to reveal what drives the observed diversity of subduction tectonics. While global correlations between some observed subduction features can be established, such as slab dip and back-arc deformation with upper plate motion and upper plate thickness, be it with notable exceptions (e.g. Lallemand et al., 2005; Heuret & Lallemand, 2005), many other parameters have poor correlations (e.g. Cruciani et al., 2005; Doglioni et al., 2007; Vérard et al., 2015). Our results demonstrate the ability of slab remnants to significantly enhance sinking velocities and affect trench motion. It is therefore likely that the effect of mantle flow driven by subducted remnants contributes to an explanation for these poor correlations.

One of our key findings is that the downwelling flow generated by negatively buoyant slab remnants can enhance the descent of nearby subducting plates. Numerical models have suggested that slab sinking velocity should increase with plate age, which enhances slab pull (e.g., Goes et al., 2011; Garel et al., 2014; Agrusta et al., 2017; F. Chen et al., 2022b). Nonetheless, despite there being some positive velocity-age trend for larger plates (e.g. Lallemand et al., 2005; Goes et al., 2011), overall there is a poor correlation between subducting plate velocities and age (e.g., in the recent global plate reconstructions of Müller et al., 2016, 2019). This suggests that there are factors, other than age,

impacting the velocities of subducting plates, one of which may be the interaction with nearby remnants or ongoing subducting slabs. As shown in Figures 5, 9 and 11 (panel e), a nearby negatively buoyant remnant can increase slab sinking velocities. Such slab-remnant interactions would complicate the trend of measured plate velocities with subducting plate age. Likewise, interaction with remnants may provide a plausible explanation for slabs currently residing at a deeper depth than expected from tectonic reconstructions, such as the Arabia and Kalimantan slabs, as noted by van der Meer et al. (2018).

In addition to increasing slab sinking velocities, the downwelling flow driven by negatively buoyant remnants can potentially help to sustain or initiate subduction. Our results suggest that slabs and remnants tend to move towards each other, which may help to anchor and sustain subduction at a given location for a prolonged period of time. There is a strong correlation between subduction zone initiation events and the presence of nearby previous subduction (Crameri et al., 2020). Pysklywec and Ishii (2005) used 2-D numerical models to demonstrate that slab remnants may trigger slab detachment, and subsequent initiation of subduction of the opposite polarity. Nikolaeva et al. (2010) modelled subduction initiation at passive margins, and suggested the criteria for spontaneous initiation are hard to achieve naturally. Even in other settings, it seems subduction initiation usually requires additional forcing (e.g. Lallemand & Arcay, 2021). Capitanio and Replumaz (2013) modelled slab break-off, and showed that while break-off episodes provide short-lived and localised large stresses in the upper plate interior, the detached slab remnants sustained the subduction dynamics that drive convergent motion. Such dynamics could explain long-lived under thrusting at the India-Asia convergence zone and episodic lithospheric faulting in the Asian continent. Significant downwelling from detached slabs may also facilitate the continuation of subduction. For example, the remnant of the Izanagi plate may have provided the driving force for Pacific Plate subduction at the East Asian margin after the sub-parallel subduction of the Izanagi-Pacific ridge at $\sim$ 50 Ma (e.g. Seton et al., 2015; Wu & Wu, 2019).

Our models also show that remnants can influence trench shape. Observed along-strike variations in trench shape have been attributed to different factors: (i) the influence of upper plate heterogeneity (e.g. Capitanio, Stegman, et al., 2010; Arnulf et al., 2022); (ii) the impact of subducting a buoyant anomaly, such as ridges and oceanic plateaus, which resist subduction and trench retreat (e.g. Mason et al., 2010; Suchoy et al., 2022); and (iii) plate width, where the centre of a wider plate tends to retreat less than the edges, or even stagnate, resulting in a 'W'-shaped trench (e.g. Schellart et al., 2007; F. Chen et al., 2022b). Our models suggest that depending on a remnants' location relative to the subducting plate, it can either enhance trench curvature (as in case W4800_Wedge_half, Figure 10), reduce trench curvature (most notably in case W4800_Subslab_half, Figure 10), induce trench rotation towards the remnant (case Asym_Wedge_Negative, Figure 13c), or influence the location of the protruding stagnation zone along the trench (case Asym_Wedge_Negative, Figure 13c). Whilst both slab remnants and buoyant ridges could lead to localised convex curvature at the trench, there is a clear distinction between them: at the protruding centre of the trench induced by a remnant, the slab is advancing forward with a steep dip (Figure 11b,f). This differs to the stagnating trench shape induced by the subduction of a buoyant anomaly, which is associated with shallower dip angles (Suchoy et al., 2022).

Our models suggest that the coupled flow from negatively buoyant remnants and the downgoing subducting slab acts to reduce the distance between them, primarily via rotation. This rotation is seen in the increasing slab dip (panel f in Figures 5, 9 and 11) and remnant rotation in Figure 6(d,e). However, such a rotation is limited by the direction of gravity: when the remnant and slab are descending in a radial orientation aligned with gravity, they cannot rotate any further, as illustrated by case W2400_Radial, and they do not further approach. This contributes to an explanation of why many distinct

slab fragments are still imaged in the mantle (e.g., Ren et al., 2007; Wu & Suppe, 2018; Braszus et al., 2021; van der Meer et al., 2018).

Finally, it has long been recognised that super-continents assemble and break up episodically throughout Earth's history, and this cycle is intimately linked to whole-mantle convection (e.g., Nance et al., 1988; Rogers & Santosh, 2003; Nance et al., 2014; Rolf et al., 2014; Mitchell et al., 2021). In particular, the assembly stage of super-continent cycles is heavily influenced by subduction. Collins (2003) suggested that long-lived slab pull forces controlled Pangaean assembly and dispersal, whilst Santosh et al. (2009) suggested that the process of super continent assembly is driven by super-downwelling through double-sided subduction as seen in the Western Pacific. Our models suggest that the downwelling flow generated by slab remnants can concentrate the locations of slabs, leading to the potential development of super-downwellings. The negative buoyancy of these accumulated remnants may also aid subduction initiation of overlying oceanic lithosphere, which further concentrates negative buoyancy and feedbacks into potential super-downwelling systems. Therefore, based on our results, we speculate that the location and volume of remnant slabs in the mantle may be a crucial factor controlling ongoing and new subduction zones, global plate reorganisation events and super-continent cycles.

4.3 Examples of Slab-Remnant Interactions

Seismic tomography studies (e.g., Li et al., 2008; van der Meer et al., 2018) show an abundance of remnants in the mantle within close proximity to active subduction zones (see Figure 1). These regions typically have complex tectonic histories, and the results from our models may contribute towards an improved understanding of how the evolution of these subduction systems have been shaped by interactions with nearby remnants. Given that such remnants are scattered around the globe and are capable of affecting subduction zones that range in scale from the large (e.g., Tethyan and Farallon subduction) to the small (e.g. South-East Asian subduction zones), it is important to understand slab-remnant interactions. Below, we highlight a few examples of where slab-remnant interaction may have affected tectonic evolution.

Closure of the Tethys Oceans left substantial subducted remnants below a region extending from the Mediterranean subduction zones to the India-Eurasian collision. Tomographic imaging shows that slab remnants from Tethyan subduction under India are located near the ancient locations where they began subduction, and that Tethyan slab remnants are largely above previous subducted fragments, implying only small amounts of lateral movement, which is an indication of an anchored and ongoing subduction system (e.g. van der Voo et al., 1999; Hafkenscheid et al., 2006). This is similar to our W2400_Under model, where the downwelling flow from the pre-existing remnant reduces the distance between the remnant and the subducting slab and effectively pins the location of subduction (Figure 5i).

Capitanio, Morra, et al. (2010) examined the force balance required to drive reconstructed plate motions associated the India-Asia convergence, showing that these are three times higher than what can be explained by this subduction system in isolation. They suggest that this may result from the flow field created by Paleo-Tethys slabs sinking through the lower mantle. This was confirmed by Becker and Faccenna (2011), who suggested that the mantle drag exerted on the base of the lithosphere acts like a 'conveyor belt', driving ongoing indentation of the Indian and Arabian plates into Eurasia. Furthermore, the flow patterns generated by the relics of west Tethyan subduction may have aided Mediterranean subduction and its rollback (Faccenna et al., 2014). These studies, considered alongside our results, demonstrate a key role for remnant-induced mantle flow in the tectonic force-balance.

Seismic tomography models illuminate remnants of the Farallon and possibly other plates in and below the mantle transition zone below the North America plate (van der

Lee & Nolet, 1997; Goes & van der Lee, 2002; Ren et al., 2007; Sigloch et al., 2008). These remnants could have driven downwelling flow that aided scenarios where multiple basins subducted on top of each other, generating large-scale tomographic anomalies interpreted as vertical 'slab walls', and facilitating proposed subduction polarity flips (Sigloch & Mihalynuk, 2013). Remnants currently in the lower mantle below the northwestern United States have been attributed to subduction that started at an intra-oceanic arc west of the North American continental margin (e.g. Ren et al., 2007; Sigloch & Mihalynuk, 2013) and, although other factors likely contributed to the westward motion of the North America plate (e.g. Müller et al., 2019), the flow generated by these slab remnants could have aided such motion.

The Antilles and South American subduction zones are tectonically complex. The Antilles slab appears to be highly fragmented (e.g. Bezada et al., 2010; van Benthem et al., 2013; Braszus et al., 2021) and is affected by motions of the major surrounding plates. It is suggested that some Antillean slab fragments are currently located in the lower mantle beneath northeastern South America (e.g. van Benthem et al., 2013; Braszus et al., 2021). Other subducted remnants, likely from Farallon subduction, have also been identified in the mantle transition zone and lower mantle below southeastern North America (e.g. Bunge & Grand, 2000; Ren et al., 2007; Sigloch et al., 2008). Flow associated with these relic slabs could well have facilitated subduction and the penetration of Farallon and Nazca slabs into the lower mantle beneath Central America and north-central South America (e.g., van der Meer et al., 2018). Furthermore, in conjunction with the effects of plate width (e.g. Schellart, 2017; F. Chen et al., 2022b) and the subduction of buoyant anomalies (e.g. Gutscher et al., 1999; Suchoy et al., 2022), slab fragments below northern South America could have enhanced oroclinal bending of the trench at Bolivia, similar to the enhanced trench curvature predicted for case W4800_Wedge_half herein.

South East Asia has a complex tectonic history and, as a result, a complex underlying mantle structure (e.g. Replumaz et al., 2004; Hall & Spakman, 2015; van der Meer et al., 2018; Pilia et al., 2023). Material subducted along the former Banda trench forms a large flat lying remnant just below the mantle transition zone (Spakman & Hall, 2010); and despite the 'stalled' appearance of the slab, its stagnation at 660 km discontinuity may well be transient (Goes et al., 2017), in which case its negative buoyancy likely enhances subduction and sinking of the many small slabs below northeastern Indonesia and the Philippines. The remnant in the sub-slab region of the lower mantle beneath Sumatra–Andaman has been associated with Tethyan subduction (e.g. Widiyantoro & van der Hilst, 1997; Hafkenscheid et al., 2006; Spakman & Hall, 2010); and based on our results, a remnant in such a location relative to the subducting plate is likely to drive trench retreat and back-arc opening behind Andaman.

Below the Tonga-New Hebrides plate boundary, seismic tomography models suggest distinct 3-D structures that represent slab remnants from past subduction at the Melanesia Arc (e.g. W.-P. Chen & Brudzinski, 2001; Hall & Spakman, 2002). As occurs in our models, active subduction in this region is likely affected by the negative buoyancy of these remnants (Pysklywec et al., 2003; Pysklywec & Ishii, 2005). Variable sinking velocities along the subduction zone, suggested based on tectonic reconstructions (Schellart & Spakman, 2012), could be an indicator of a non-uniform, asymmetric influence from remnants, similar to the case Asym_Wedge_Negative analysed herein.

5 Conclusions

We have presented a suite of subduction models in a 3-D hemispherical shell domain, investigating how different slab remnant properties – density, size, location and orientation – influence interaction with a nearby subduction zone. We have also presented two full spherical models with an asymmetric setup, to illustrate the effect of remnants in driving asymmetric along-strike variations in trench shape and slab morphology.

Our models show that downwelling flow generated by negatively buoyant slab remnants can be of similar scale and magnitude as that of the subducting slab and when located within a few 100 to 1000 km from the slab tip, this flow enhances the sinking velocity of nearby actively subducting slabs by up to a factor 2 (depending on remnant size and location). The joint effects of remnant downwelling and slab pull may explain the observed poor correlations between subducting plate velocities and the age of the subducting lithosphere.

The location of a remnant relative to a nearby subduction system can be an important factor controlling the evolution of trench shape. Sinking remnants and subducting slabs move towards each other via rotation, leading to increasing alignment of the flow set up by the slab and remnant. Remnants located in the sub-slab region, under the incoming plate, tend enhance trench retreat, whereas remnants on the mantle wedge side facilitate trench advance. For wide subduction zones in particular, which develop a convex trench stagnation/advance zone at their centre, the mantle flow field generated by a sinking remnant can influence along-strike trench shape variation and potentially drive the convex stagnation point away from the centre of the trench towards the remnant. This process may have contributed to trench evolution in regions such as the Bolivian Orocline above the Nazca subduction system.

With the abundance of relic subduction fragments that have been identified in mantle tomography, and examples of interactions with subduction zones around the globe, we suggest that slab-remnant interaction is an important process that influences subduction dynamics on Earth, significantly affecting plate velocities and trench shapes. Remnants likely also help to anchor and sustain subduction systems, and facilitate subduction initiation events that drive large-scale plate reorganisations and super-continent cycles.

Open Research

The Fluidity computational modelling framework, including source code and documentation, is available from `https://fluidityproject.github.io/`; the version used for the simulations presented herein has been archived at Kramer, Wilson, et al. (2021). The input files required to reproduce the simulations presented herein have also been made available at F. Chen (2023). Figures have been prepared using Matplotlib, Cartopy and Paraview. Figure 1 was prepared using SubMachine (Hosseini et al., 2018).

Acknowledgments

F.C. is funded by an Australian Government Research Training Program (RTP) Scholarship. D.R.D. and S.C.K. acknowledge support from the Australian Research Council (ARC) under DP170100058, the Australian Research Data Commons (ARDC, under the G-Adopt platform grant: PL031), AuScope, Geosciences Australia and the National Computational Infrastructure (NCI). L.S. was funded by an EPSRC DTP studentship (EP/N509486/1), S.G. received support under NERC grant NE/K010743/1. This research was supported by the Australian Government's National Collaborative Research Infrastructure Strategy (NCRIS), with access to computational resources provided on Gadi through the National Computational Merit Allocation Scheme and the ANU Merit Allocation Scheme. Authors would like to thank Cian Wilson, Chris Matthews, Thomas Duvernay, Siavash Ghelichkhan, Mark Hoggard and Angus Gibson for fruitful discussions at various stages of this research.

References

Abratis, M., & Wörner, G. (2001). Ridge collision, slab-window formation, and the flux of Pacific asthenosphere into the Caribbean realm. *Geology*, *29*(2), 127–

130.

Agrusta, R., Goes, S., & van Hunen, J. (2017). Subducting-slab transition-zone interaction: Stagnation, penetration and mode switches. *Earth and Planetary Science Letters*, *464*, 10–23. doi: 10.1016/j.epsl.2017.02.005

Amaru, M. L. (2007). *Global travel time tomography with 3-D reference models* (Vol. 274). Utrecht University.

Andrews, E. R., & Billen, M. I. (2009). Rheologic controls on the dynamics of slab detachment. *Tectonophysics*, *464*(1-4), 60–69.

Arnulf, A. F., Bassett, D., Harding, A. J., Kodaira, S., Nakanishi, A., & Moore, G. (2022). Upper-plate controls on subduction zone geometry, hydration and earthquake behaviour. *Nature Geoscience*, *15*(2), 143–148.

Becker, T. W., & Faccenna, C. (2011). Mantle conveyor beneath the Tethyan collisional belt. *Earth and Planetary Science Letters*, *310*(3-4), 453–461. doi: 10.1016/j.epsl.2011.08.021

Becker, T. W., & O'Connell, R. J. (2001). Predicting plate velocities with mantle circulation models. *Geochemistry, Geophysics, Geosystems*, *2*(12). doi: https://doi.org/10.1029/2001GC000171

Bellahsen, N., Faccenna, C., & Funiciello, F. (2005). Dynamics of subduction and plate motion in laboratory experiments: Insights into the "plate tectonics" behavior of the Earth. *Journal of Geophysical Research: Solid Earth*, *110*(B1). doi: 10.1029/2004JB002999

Bezada, M. J., Levander, A., & Schmandt, B. (2010). Subduction in the southern Caribbean: Images from finite-frequency P-wave tomography. *Journal of Geophysical Research: Solid Earth*, *115*(B12). doi: https://doi.org/10.1029/2010JB007682

Bijwaard, H., Spakman, W., & Engdahl, E. R. (1998). Closing the gap between regional and global travel time tomography. *Journal of Geophysical Research: Solid Earth*, *103*(B12), 30055–30078.

Braszus, B., Goes, S., Allen, R., Rietbrock, A., Collier, J., Harmon, N., ... others (2021). Subduction history of the Caribbean from upper-mantle seismic imaging and plate reconstruction. *Nature communications*, *12*(1), 1–14.

Bunge, H.-P., & Grand, S. P. (2000). Mesozoic plate-motion history below the northeast Pacific Ocean from seismic images of the subducted Farallon slab. *Nature*, *405*(6784), 337–340.

Bunge, H.-P., Richards, M. A., & Baumgardner, J. R. (2002). Mantle circulation models with sequential data-assimilation: inferring present-day mantle structure from plate motion histories. *Phil. Trans. R. Soc. London, Set. A*, *360*, 2545–2567. doi: 10.1098/rsta.2002.1080.

Burkett, E. R., & Billen, M. I. (2009). Dynamics and implications of slab detachment due to ridge-trench collision. *Journal of Geophysical Research: Solid Earth*, *114*(B12).

Capitanio, F. A. (2013). Lithospheric-age control on the migrations of oceanic convergent margins. *Tectonophysics*, *593*, 193-200. doi: https://doi.org/10.1016/j.tecto.2013.03.003

Capitanio, F. A., Faccenna, C., & Funiciello, R. (2009). The opening of Sirte basin: Result of slab avalanching? *Earth and Planetary Science Letters*, *285*(1-2), 210–216. doi: 10.1016/j.epsl.2009.06.019

Capitanio, F. A., Morra, G., & Goes, S. (2007). Dynamic models of downgoing plate-buoyancy driven subduction: Subduction motions and energy dissipation. *Earth and Planetary Science Letters*, *262*(1-2), 284–297. doi: 10.1016/j.epsl.2007.07.039

Capitanio, F. A., Morra, G., Goes, S., Weinberg, R. F., & Moresi, L. N. (2010). India–Asia convergence driven by the subduction of the Greater Indian continent. *Nature Geoscience*, *3*(2), 136–139.

Capitanio, F. A., & Replumaz, A. (2013). Subduction and slab breakoff controls on

Asian indentation tectonics and Himalayan western syntaxis formation. *Geochemistry, Geophysics, Geosystems*, *14*(9), 3515–3531.

Capitanio, F. A., Stegman, D. R., Moresi, L. N., & Sharples, W. (2010). Upper plate controls on deep subduction, trench migrations and deformations at convergent margins. *Tectonophysics*, *483*(1-2), 80–92. doi: 10.1016/j.tecto.2009.08.020

Cerpa, N. G., Sigloch, K., Garel, F., Heuret, A., Davies, D. R., & Mihalynuk, M. (2022). The effect of a weak asthenospheric layer on surface kinematics, subduction dynamics and slab morphology in the lower mantle. *J. Geophys. Res.*, *127*, e2022JB024494. doi: 10.1029/2022JB024494

Chen, F. (2023, July). *cfq2738/The-role-of-slab-remnants-in-modulating-the-dynamics-of-free-subduction: Submission.* Zenodo. Retrieved from `https://doi.org/10.5281/zenodo.8197430` doi: 10.5281/zenodo.8197430

Chen, F., Davies, D. R., Goes, S., Suchoy, L., & Kramer, S. C. (2022a). Comparing the Dynamics of Free Subduction in Cartesian and Spherical Domains. *Geochemistry, Geophysics, Geosystems*, e2022GC010757. doi: 10.1029/2022GC010757

Chen, F., Davies, D. R., Goes, S., Suchoy, L., & Kramer, S. C. (2022b). How slab age and width combine to dictate the dynamics and evolution of subduction systems: A 3-D spherical study. *Geochemistry, Geophysics, Geosystems*, e2022GC010597. doi: 10.1029/2022GC010597

Chen, W.-P., & Brudzinski, M. R. (2001). Evidence for a large-scale remnant of subducted lithosphere beneath Fiji. *Science*, *292*(5526), 2475–2479.

Chertova, M. V., Spakman, W., & Steinberger, B. (2018). Mantle flow influence on subduction evolution. *Earth and Planetary Science Letters*, *489*, 258–266. doi: 10.1016/j.epsl.2018.02.038

Christensen, U. R., & Yuen, D. A. (1984). The interaction of a subducting lithospheric slab with a chemical or phase boundary. *Journal of Geophysical Research: Solid Earth*, *89*(B6), 4389–4402.

Čížková, H., & Bina, C. R. (2019). Linked influences on slab stagnation: Interplay between lower mantle viscosity structure, phase transitions, and plate coupling. *Earth and Planetary Science Letters*, *509*, 88–99. doi: 10.1016/j.epsl.2018.12.027

Collins, W. (2003). Slab pull, mantle convection, and Pangaean assembly and dispersalx. *Earth and Planetary Science Letters*, *205*(3-4), 225–237.

Crameri, F., Magni, V., Domeier, M., Shephard, G. E., Chotalia, K., Cooper, G., ... others (2020). A trans-disciplinary and community-driven database to unravel subduction zone initiation. *Nature communications*, *11*(1), 1–14.

Cruciani, C., Carminati, E., & Doglioni, C. (2005). Slab dip vs. lithosphere age: no direct function. *Earth and Planetary Science Letters*, *238*(3-4), 298–310.

Davies, D. R., Ghelichkhan, S., Hoggard, M., Valentine, A. P., & Richards, F. D. (2023). Observations and models of dynamic topography: Current status and future directions. *Dynamics of Plate Tectonics and Mantle Convection*, 223–269.

Davies, D. R., Goes, S., Davies, J. H., Schuberth, B. S. A., Bunge, H., & Ritsema, J. (2012). Reconciling dynamic and seismic models of Earth's lower mantle: the dominant role of thermal heterogene ity. *Earth Planet. Sci. Lett.*, *353–354*, 253–269. doi: 10.1016/j.epsl.2012.08.016

Davies, D. R., Goes, S., & Lau, H. C. P. (2015). Thermally Dominated Deep Mantle LLSVPs: A Review. In A. Khan & F. Deschamps (Eds.), *The Earth's Heterogeneous Mantle* (p. 441-477). Springer International Publishing. doi: 10.1007/978-3-319-15627-9_14

Davies, D. R., Le Voci, G., Goes, S., Kramer, S. C., & Wilson, C. R. (2016). The mantle wedge's transient 3-D flow regime and thermal structure. *Geochem. Geophys. Geosys.*, *17*, 78-100. doi: 10.1002/2015GC006125

Davies, D. R., Wilson, C. R., & Kramer, S. C. (2011). Fluidity: A fully unstruc-

tured anisotropic adaptive mesh computational modeling framework for geodynamics. *Geochemistry, Geophysics, Geosystems*, *12*(6), 253-269. doi: 10.1029/2011GC003551

Davies, J. H., & von Blanckenburg, F. (1995). Slab breakoff: a model of lithosphere detachment and its test in the magmatism and deformation of collisional orogens. *Earth and Planetary Science Letters*, *129*(1-4), 85–102.

Doglioni, C., Carminati, E., Cuffaro, M., & Scrocca, D. (2007). Subduction kinematics and dynamic constraints. *Earth-Science Reviews*, *83*(3-4), 125–175.

Duretz, T., Gerya, T., & Spakman, W. (2014). Slab detachment in laterally varying subduction zones: 3-D numerical modeling. *Geophysical Research Letters*, *41*(6), 1951–1956.

Faccenna, C., Becker, T. W., Auer, L., Billi, A., Boschi, L., Brun, J. P., ... Serpelloni, E. (2014). Mantle dynamics in the Mediterranean. *Reviews of Geophysics*, *52*(3), 283-332. doi: https://doi.org/10.1002/2013RG000444

Faccenna, C., Bellier, O., Martinod, J., Piromallo, C., & Regard, V. (2006). Slab detachment beneath eastern Anatolia: A possible cause for the formation of the North Anatolian fault. *Earth and Planetary Science Letters*, *242*(1-2), 85–97.

Ficini, E., Dal Zilio, L., Doglioni, C., & Gerya, T. (2017). Horizontal mantle flow controls subduction dynamics. *Scientific Reports*, *7*(1), 7550.

Forsyth, D., & Uyeda, S. (1975). On the relative importance of the driving forces of plate motion. *Geophysical Journal International*, *43*(1), 163–200. doi: 10.1111/j.1365-246X.1975.tb00631.x

Fukao, Y., & Obayashi, M. (2013). Subducted slabs stagnant above, penetrating through, and trapped below the 660 km discontinuity. *Journal of Geophysical Research: Solid Earth*, *118*(11), 5920–5938. doi: 10.1002/2013JB010466

Fukao, Y., Obayashi, M., Nakakuki, T., & Group, D. S. P. (2009). Stagnant slab: a review. *Annual Review of Earth and Planetary Sciences*, *37*, 19–46.

Garel, F., Goes, S., Davies, D. R., Davies, J. H., Kramer, S. C., & Wilson, C. R. (2014). Interaction of subducted slabs with the mantle transition-zone: A regime diagram from 2-D thermo-mechanical models with a mobile trench and an overriding plate. *Geochemistry, Geophysics, Geosystems*, *15*(5), 1739–1765. doi: 10.1002/2014GC005257

Ghelichkhan, S., Bunge, H., & Oeser, J. (2021). Global mantle flow retrodictions for the early Cenozoic using an adjoint method: evolving dynamic topographies, deep mantle structures, flow trajectories and sublithospheric stresses. *Geophysical Journal International*, *226*(2), 1432–1460.

Goes, S., Agrusta, R., van Hunen, J., & Garel, F. (2017). Subduction-transition zone interaction: A review. *Geosphere*, *13*(3), 644–664. doi: 10.1130/GES01476.1

Goes, S., Capitanio, F. A., Morra, G., Seton, M., & Giardini, D. (2011). Signatures of downgoing plate-buoyancy driven subduction in Cenozoic plate motions. *Physics of the Earth and Planetary Interiors*, *184*(1-2), 1–13. doi: 10.1016/j.pepi.2010.10.007

Goes, S., & van der Lee, S. (2002). Thermal structure of the north american uppermost mantle inferred from seismic tomography. *Journal of Geophysical Research: Solid Earth*, *107*(B3), ETG 2-1-ETG 2-13. doi: https://doi.org/10.1029/2000JB000049

Gorbatov, A., Widiyantoro, S., Fukao, Y., & Gordeev, E. (2000). Signature of remnant slabs in the North Pacific from P-wave tomography. *Geophysical Journal International*, *142*(1), 27–36.

Govers, R., & Wortel, M. (2005). Lithosphere tearing at step faults: Response to edges of subduction zones. *Earth and Planetary Science Letters*, *236*(1-2), 505–523.

Grand, S. P., Van der Hilst, R. D., & Widiyantoro, S. (1997). High resolution global tomography: a snapshot of convection in the Earth. *Geological Society of*

America Today, *7*(4).

Gutscher, M. A., Olivet, J. L., Aslanian, D., Eissen, J. P., & Maury, R. (1999). The "Lost Inca Plateau": Cause of flat subduction beneath Peru? *Earth and Planetary Science Letters*, *171*(3), 335–341. doi: 10.1016/S0012-821X(99)00153-3

Hafkenscheid, E., Wortel, M., & Spakman, W. (2006). Subduction history of the Tethyan region derived from seismic tomography and tectonic reconstructions. *Journal of geophysical research: Solid Earth*, *111*(B8).

Hager, B. H. (1984). Subducted slabs and the geoid: Constraints on mantle rheology and flow. *Journal of Geophysical Research: Solid Earth*, *89*(B7), 6003–6015.

Hager, B. H., & O'Connell, R. J. (1979). Kinematic models of large-scale flow in the Earth's mantle. *Journal of Geophysical Research: Solid Earth*, *84*(B3), 1031–1048.

Hager, B. H., & Richards, A. M. (1989). Long–wavelength variations in Earth's geoid: Physical models and dynamical implications. *Phil. Trans. Roy. Soc. London, Ser. A.*, *328*, 309–327.

Hall, R., & Spakman, W. (2002). Subducted slabs beneath the eastern Indonesia–Tonga region: insights from tomography. *Earth and Planetary Science Letters*, *201*(2), 321–336.

Hall, R., & Spakman, W. (2015). Mantle structure and tectonic history of SE Asia. *Tectonophysics*, *658*, 14–45.

Heuret, A., Funiciello, F., Faccenna, C., & Lallemand, S. (2007). Plate kinematics, slab shape and back-arc stress: A comparison between laboratory models and current subduction zones. *Earth and Planetary Science Letters*, *256*(3-4), 473–483. doi: 10.1016/j.epsl.2007.02.004

Heuret, A., & Lallemand, S. (2005). Plate motions, slab dynamics and back-arc deformation. *Physics of the Earth and Planetary Interiors*, *149*(1-2), 31–51.

Holt, A. F., & Royden, L. H. (2020). Subduction dynamics and mantle pressure: 2. towards a global understanding of slab dip and upper mantle circulation. *Geochemistry, Geophysics, Geosystems*, *21*(7), e2019GC008771.

Holt, A. F., Royden, L. H., & Becker, T. W. (2017). The dynamics of double slab subduction. *Geophysical Journal International*, *209*(1), 250–265. doi: 10.1093/gji/ggw496

Hosseini, K., Matthews, K. J., Sigloch, K., Shephard, G. E., Domeier, M., & Tsekhmistrenko, M. (2018). SubMachine: Web-based tools for exploring seismic tomography and other models of Earth's deep interior. *Geochemistry, Geophysics, Geosystems*, *19*(5), 1464–1483.

Hu, J., & Gurnis, M. (2020). Subduction duration and slab dip. *Geochemistry, Geophysics, Geosystems*, *21*(4), e2019GC008862.

Husson, L. (2012). Trench migration and upper plate strain over a convecting mantle. *Physics of the Earth and Planetary Interiors*, *212*, 32–43.

Ito, E., & Yamada, H. (1982). Stability relations of silicate spinels, ilmenites, and perovskites. In S. Akimoto & M. H. Manghnani (Eds.), *High-pressure research in geophysics* (pp. 405–419).

Jarrard, R. D. (1986). Relations among subduction parameters. *Reviews of Geophysics*, *24*(2), 217–284. doi: 10.1029/RG024i002p00217

Jarvis, G. T., & Lowman, J. P. (2007). Survival times of subducted slab remnants in numerical models of mantle flow. *Earth and Planetary Science Letters*, *260*(1-2), 23–36.

Karato, S.-i., Riedel, M. R., & Yuen, D. A. (2001). Rheological structure and deformation of subducted slabs in the mantle transition zone: Implications for mantle circulation and deep earthquakes. *Physics of the Earth and Planetary Interiors*, *127*(1-4), 83–108.

Kramer, S. C., Davies, D. R., & Wilson, C. R. (2021). Analytical solutions for mantle flow in cylindrical and spherical shells. *Geoscientific Model Development*, *14*(4), 1899–1919. doi: 10.5194/gmd-14-1899-2021

Kramer, S. C., Wilson, C., Funke, S. W., Greaves, T., Avdis, A., Davies, R., ... Ham, D. A. (2021). *FluidityStokes/fluidity: Spherical Adaptivity branch.* Zenodo. Retrieved from `https://doi.org/10.5281/zenodo.5636819` doi: 10.5281/zenodo.5636819

Kramer, S. C., Wilson, C. R., & Davies, D. R. (2012). An implicit free surface algorithm for geodynamical simulations. *Physics of the Earth and Planetary Interiors*, *194*, 25–37. doi: 10.1016/j.pepi.2012.01.001

Kundu, B., & Santosh, M. (2011). Dynamics of post-slab breakoff in convergent plate margins: a "jellyfish" model. *American Journal of Science*, *311*(8), 701–717.

Lallemand, S., & Arcay, D. (2021). Subduction initiation from the earliest stages to self-sustained subduction: Insights from the analysis of 70 cenozoic sites. *Earth-Science Reviews*, *221*, 103779.

Lallemand, S., Heuret, A., & Boutelier, D. (2005). On the relationships between slab dip, back-arc stress, upper plate absolute motion, and crustal nature in subduction zones. *Geochemistry, Geophysics, Geosystems*, *6*(9), Q09006. doi: 10.1029/2005GC000917

Lei, W., Ruan, Y., Bozdağ, E., Peter, D., Lefebvre, M., Komatitsch, D., ... Pugmire, D. (2020). Global adjoint tomography—model glad-m25. *Geophysical Journal International*, *223*(1), 1–21.

Le Voci, G., Davies, D. R., Goes, S., Kramer, S. C., & Wilson, C. R. (2014). A systematic 2-D investigation into the mantle wedge's transient flow regime and thermal structure: complexities arising from a hydrated rheology and thermal buoyancy. *Geochem. Geophys. Geosys.*, *15*, 28–51. doi: 10.1002/2013GC005022

Li, C., van der Hilst, R. D., Engdahl, E. R., & Burdick, S. (2008). A new global model for P wave speed variations in Earth's mantle. *Geochemistry, Geophysics, Geosystems*, *9*(5).

Lithgow-Bertelloni, C., & Richards, M. A. (1998). The dynamics of Cenozoic and Mesozoic plate motions. *Reviews of Geophysics*, *36*(1), 27–78. doi: 10.1029/97RG02282

Lowman, J. P. (2011). Mantle convection models featuring plate tectonic behavior: An overview of methods and progress. *Tectonophysics*, *510*(1-2), 1–16.

Mason, W. G., Moresi, L., Betts, P. G., & Miller, M. S. (2010). Three-dimensional numerical models of the influence of a buoyant oceanic plateau on subduction zones. *Tectonophysics*, *483*(1-2), 71–79. doi: 10.1016/j.tecto.2009.08.021

Matthews, K. J., Seton, M., & Müller, R. D. (2012). A global-scale plate reorganization event at 105–100 Ma. *Earth and Planetary Science Letters*, *355*, 283–298. doi: 10.1016/j.epsl.2012.08.023

Mitchell, R. N., Zhang, N., Salminen, J., Liu, Y., Spencer, C. J., Steinberger, B., ... Li, Z.-X. (2021). The supercontinent cycle. *Nature Reviews Earth & Environment*, *2*(5), 358–374.

Müller, R. D., Seton, M., Zahirovic, S., Williams, S. E., Matthews, K. J., Wright, N. M., ... Cannon, J. (2016). Ocean basin evolution and global-scale plate reorganization events since Pangea breakup. *Annual Review of Earth and Planetary Sciences*, *44*, 107–138. doi: 10.1146/annurev-earth-060115-012211

Müller, R. D., Zahirovic, S., Williams, S. E., Cannon, J., Seton, M., Bower, D. J., ... Gurnis, M. (2019). A global plate model including lithospheric deformation along major rifts and orogens since the Triassic. *Tectonics*, *38*(6), 1884–1907. doi: 10.1029/2018TC005462

Nance, R. D., Murphy, J. B., & Santosh, M. (2014). The supercontinent cycle: a retrospective essay. *Gondwana Research*, *25*(1), 4–29.

Nance, R. D., Worsley, T. R., & Moody, J. B. (1988). The supercontinent cycle. *Scientific American*, *259*(1), 72–79.

Nikolaeva, K., Gerya, T., & Marques, F. (2010). Subduction initiation at passive

margins: Numerical modeling. *Journal of Geophysical Research: Solid Earth*, *115*(B3).

Obayashi, M., Yoshimitsu, J., & Fukao, Y. (2009). Tearing of stagnant slab. *Science*, *324*(5931), 1173–1175.

OzBench, M., Regenauer-Lieb, K., Stegman, D. R., Morra, G., Farrington, R., Hale, A., ... Moresi, L. (2008). A model comparison study of large-scale mantle–lithosphere dynamics driven by subduction. *Physics of the Earth and Planetary Interiors*, *171*(1-4), 224–234. doi: 10.1016/j.pepi.2008.08.011

Pallares, C., Maury, R. C., Bellon, H., Royer, J.-Y., Calmus, T., Aguillón-Robles, A., ... Bourgois, J. (2007). Slab-tearing following ridge-trench collision: Evidence from Miocene volcanism in Baja California, México. *Journal of Volcanology and Geothermal Research*, *161*(1-2), 95–117.

Pilia, S., Davies, D. R., Hall, R., Bacon, C. A., Gilligan, A., Greenfield, T., ... others (2023). Post-subduction tectonics induced by extension from a lithospheric drip. *Nature Geoscience*, 1–7.

Piromallo, C., Becker, T., Funiciello, F., & Faccenna, C. (2006). Three-dimensional instantaneous mantle flow induced by subduction. *Geophysical Research Letters*, *33*(8). doi: 10.1029/2005GL025390

Pysklywec, R. N., & Ishii, M. (2005). Time dependent subduction dynamics driven by the instability of stagnant slabs in the transition zone. *Physics of the Earth and Planetary Interiors*, *149*(1-2), 115–132. doi: 10.1016/j.pepi.2004.08.019

Pysklywec, R. N., & Mitrovica, J. X. (1999). The role of subduction-induced subsidence in the evolution of the Karoo Basin. *The Journal of Geology*, *107*(2), 155–164. doi: 10.1086/314338

Pysklywec, R. N., Mitrovica, J. X., & Ishii, M. (2003). Mantle avalanche as a driving force for tectonic reorganization in the southwest Pacific. *Earth and Planetary Science Letters*, *209*(1-2), 29–38. doi: 10.1016/S0012-821X(03)00073-6

Quéré, S., Lowman, J., Arkani-Hamed, J., Roberts, J., & Moucha, R. (2013). Subcontinental sinking slab remnants in a spherical geometry mantle model. *Journal of Geophysical Research: Solid Earth*, *118*(4), 1760–1777.

Ren, Y., Stutzmann, E., van der Hilst, R. D., & Besse, J. (2007). Understanding seismic heterogeneities in the lower mantle beneath the Americas from seismic tomography and plate tectonic history. *Journal of Geophysical Research: Solid Earth*, *112*(B1). doi: https://doi.org/10.1029/2005JB004154

Replumaz, A., Karason, H., van der Hilst, R. D., Besse, J., & Tapponnier, P. (2004). 4-D evolution of SE Asia's mantle from geological reconstructions and seismic tomography. *Earth and Planetary Science Letters*, *221*(1-4), 103–115.

Ribe, N. M. (2010). Bending mechanics and mode selection in free subduction: A thin-sheet analysis. *Geophysical Journal International*, *180*(2), 559–576. doi: 10.1111/j.1365-246X.2009.04460.x

Ringwood, A. E. (1975). Composition and Petrology of the Earth's Mantle. *MacGraw-Hill*, 618.

Rogers, J. J., & Santosh, M. (2003). Supercontinents in Earth history. *Gondwana Research*, *6*(3), 357–368.

Rolf, T., Coltice, N., & Tackley, P. J. (2014). Statistical cyclicity of the supercontinent cycle. *Geophysical Research Letters*, *41*(7), 2351–2358.

Rubey, M., Brune, S., Heine, C., Davies, D. R., Williams, S. E., & Müller, R. D. (2017). Global patterns in Earth's dynamic topography since the Jurassic: the role of subducted slabs. *Solid Earth*, *8*, 899-919. doi: 10.5194/se-8-899-2017

Santosh, M., Maruyama, S., & Yamamoto, S. (2009). The making and breaking of supercontinents: some speculations based on superplumes, super downwelling and the role of tectosphere. *Gondwana Research*, *15*(3-4), 324–341.

Schellart, W. P. (2017). Andean mountain building and magmatic arc migration driven by subduction-induced whole mantle flow. *Nature communications*, *8*(1), 1–13. doi: 10.1038/s41467-017-01847-z

Schellart, W. P., Freeman, J., Stegman, D. R., Moresi, L., & May, D. (2007). Evolution and diversity of subduction zones controlled by slab width. *Nature*, *446*(7133), 308–311. doi: 10.1038/nature05615

Schellart, W. P., & Spakman, W. (2012). Mantle constraints on the plate tectonic evolution of the Tonga–Kermadec–Hikurangi subduction zone and the South Fiji Basin region. *Australian Journal of Earth Sciences*, *59*(6), 933–952.

Seton, M., Flament, N., Whittaker, J., Müller, R. D., Gurnis, M., & Bower, D. J. (2015). Ridge subduction sparked reorganization of the Pacific plate-mantle system 60–50 million years ago. *Geophysical Research Letters*, *42*(6), 1732-1740. doi: 10.1002/2015GL063057

Sigloch, K., McQuarrie, N., & Nolet, G. (2008). Two-stage subduction history under North America inferred from multiple-frequency tomography. *Nature Geoscience*, *1*(7), 458–462.

Sigloch, K., & Mihalynuk, M. G. (2013). Intra-oceanic subduction shaped the assembly of cordilleran north america. *Nature*, *496*(7443), 50–56.

Simmons, N. A., Myers, S. C., Johannesson, G., & Matzel, E. (2012). Llnl-g3dv3: Global p wave tomography model for improved regional and teleseismic travel time prediction. *Journal of Geophysical Research: Solid Earth*, *117*(B10).

Spakman, W., & Hall, R. (2010). Surface deformation and slab–mantle interaction during banda arc subduction rollback. *Nature Geoscience*, *3*(8), 562–566.

Stadler, G., Gurnis, M., Burstedde, C., Wilcox, L. C., Alisic, L., & Ghattas, O. (2010). The dynamics of plate tectonics and mantle flow: From local to global scales. *Science*, *329*(5995), 1033–1038.

Stegman, D. R., Farrington, R., Capitanio, F. A., & Schellart, W. P. (2010). A regime diagram for subduction styles from 3-D numerical models of free subduction. *Tectonophysics*, *483*(1-2), 29–45. doi: 10.1016/j.tecto.2009.08.041

Stotz, I. L., Iaffaldano, G., & Davies, D. R. (2018). Pressure-Driven Poiseuille Flow: A Major Component of the Torque-Balance Governing Pacific Plate Motion. *Geophys. Res. Lett.*, *45*, 117-125. doi: 10.1002/2017GL075697

Suchoy, L., Goes, S., Chen, F., & Davies, D. R. (2022). How aseismic ridges modify the dynamics of free subduction: a 3-D numerical investigation. *Frontiers in Earth Science*, *10*, 106. doi: 10.3389/feart.2022.852742

Suchoy, L., Goes, S., Maunder, B., Garel, F., & Davies, D. R. (2021). Effects of basal drag on subduction dynamics from 2D numerical models. *Solid Earth*, *12*(1), 79–93. doi: 10.5194/se-12-79-2021

Tackley, P. J., Stevenson, D. J., Glatzmaier, G. A., & Schubert, G. (1993). Effects of an endothermic phase transition at 670 km depth in a spherical model of convection in the Earth's mantle. *Nature*, *361*(6414), 699–704.

Thorkelson, D. J. (1996). Subduction of diverging plates and the principles of slab window formation. *Tectonophysics*, *255*(1-2), 47–63.

Thorkelson, D. J., & Taylor, R. P. (1989). Cordilleran slab windows. *Geology*, *17*(9), 833–836.

Torii, Y., & Yoshioka, S. (2007). Physical conditions producing slab stagnation: Constraints of the Clapeyron slope, mantle viscosity, trench retreat, and dip angles. *Tectonophysics*, *445*(3-4), 200–209. doi: 10.1016/j.tecto.2007.08.003

Tosi, N., Stein, C., Noack, L., Hüttig, C., Maierová, P., Samuel, H., ... Tackley, P. J. (2015). A community benchmark for viscoplastic thermal convection in a 2-d square box. *Geochemistry, Geophysics, Geosystems*, *16*(7), 2175-2196. doi: 10.1002/2015GC005807

van Benthem, S., Govers, R., Spakman, W., & Wortel, R. (2013). Tectonic evolution and mantle structure of the Caribbean. *Journal of Geophysical Research: Solid Earth*, *118*(6), 3019-3036. doi: https://doi.org/10.1002/jgrb.50235

van der Hilst, R. D., Widiyantoro, S., & Engdahl, E. (1997). Evidence for deep mantle circulation from global tomography. *Nature*, *386*(6625), 578–584.

van der Lee, S., & Nolet, G. (1997). Upper mantle S velocity structure of North

America. *Journal of Geophysical Research: Solid Earth*, *102*(B10), 22815-22838. doi: https://doi.org/10.1029/97JB01168

van der Meer, D. G., van Hinsbergen, D. J., & Spakman, W. (2018). Atlas of the underworld: Slab remnants in the mantle, their sinking history, and a new outlook on lower mantle viscosity. *Tectonophysics*, *723*, 309–448. doi: 10.1016/j.tecto.2017.10.004

van der Voo, R., Spakman, W., & Bijwaard, H. (1999). Tethyan subducted slabs under India. *Earth and Planetary Science Letters*, *171*(1), 7–20.

van Dinther, Y., Morra, G., Funiciello, F., & Faccenna, C. (2010). Role of the overriding plate in the subduction process: Insights from numerical models. *Tectonophysics*, *484*(1-4), 74–86. doi: 10.1016/j.tecto.2009.08.038

van Hunen, J., van den Berg, A. P., & Vlaar, N. J. (2001). Latent heat effects of the major mantle phase transitions on low-angle subduction. *Earth and Planetary Science Letters*, *190*(3-4), 125–135.

Verard, C. (2019). Plate tectonic modelling: review and perspectives. *Geological Magazine*, *156*(2), 208–241.

Vérard, C., Hochard, C., Baumgartner, P. O., Stampfli, G. M., & Liu, M. (2015). Geodynamic evolution of the Earth over the Phanerozoic: Plate tectonic activity and palaeoclimatic indicators. *Journal of Palaeogeography*, *4*(2), 167–188.

Wei, W., Zhao, D., Xu, J., Wei, F., & Liu, G. (2015). P and S wave tomography and anisotropy in Northwest Pacific and East Asia: Constraints on stagnant slab and intraplate volcanism. *Journal of Geophysical Research: Solid Earth*, *120*(3), 1642–1666.

Whittaker, J. M., Müller, R. D., Leitchenkov, G., Stagg, H., Sdrolias, M., Gaina, C., & Goncharov, A. (2007). Major Australian-Antarctic plate reorganization at Hawaiian-Emperor bend time. *Science*, *318*(5847), 83–86.

Widiyantoro, S., Pesicek, J., & Thurber, C. (2011). Subducting slab structure below the eastern Sunda arc inferred from non-linear seismic tomographic imaging. *Geological Society, London, Special Publications*, *355*(1), 139–155.

Widiyantoro, S., & van der Hilst, R. (1997). Mantle structure beneath Indonesia inferred from high-resolution tomographic imaging. *Geophysical Journal International*, *130*(1), 167–182.

Wong A Ton, S., & Wortel, M. (1997). Slab detachment in continental collision zones: an analysis of controlling parameters. *Geophysical Research Letters*, *24*(16), 2095–2098.

Wortel, M., & Spakman, W. (2000). Subduction and slab detachment in the Mediterranean-Carpathian region. *Science*, *290*(5498), 1910–1917.

Wu, J., & Suppe, J. (2018). Proto-South China Sea plate tectonics using subducted slab constraints from tomography. *Journal of Earth Science*, *29*(6), 1304–1318.

Wu, J., & Wu, J. (2019, 08). Izanagi-Pacific ridge subduction revealed by a 56 to 46 Ma magmatic gap along the northeast Asian margin. *Geology*, *47*(10), 953-957. doi: 10.1130/G46778.1

Yanagisawa, T., Yamagishi, Y., Hamano, Y., & Stegman, D. R. (2010). Mechanism for generating stagnant slabs in 3-D spherical mantle convection models at Earth-like conditions. *Physics of the Earth and Planetary Interiors*, *183*(1-2), 341–352.

Yang, T., Gurnis, M., & Zahirovic, S. (2018). Slab avalanche-induced tectonics in self-consistent dynamic models. *Tectonophysics*, *746*, 251–265.

Zahirovic, S., Seton, M., & Müller, R. (2014). The Cretaceous and Cenozoic tectonic evolution of Southeast Asia. *Solid Earth*, *5*(1), 227–273.

Zhao, D. (2004). Global tomographic images of mantle plumes and subducting slabs: insight into deep Earth dynamics. *Physics of the Earth and Planetary Interiors*, *146*(1-2), 3–34.